



NUMERICAL STUDY AND MODEL VALIDATION OF HEAT TRANSFER IN TURBULENT BUBBLY FLOWS

STUDENT: MATHIS GROSSO – 4012931

SUPERVISORS AND PHD CO-WORKER: G.BOIS (CEA), A.SONOLET (CEA,
PHD), R.KNIKKER (INSA)

Department of Mechanical Engineering
National Institute of Applied Sciences Lyon (INSA), *the University of Lyon*
20 avenue Albert Einstein
Villeurbanne

January 2021

A dissertation submitted to the University of Lyon in partial fulfilment of the
requirements for the degree of master

Declaration

I have read and I understand the plagiarism provisions in the General Regulations of the University Calendar for the current year.

Mathis GROSSO, January 2021

Personal comments and acknowledgements

I undertook my first experience with bubbly flows in Ireland during my master's thesis at Trinity College Dublin. I was focusing on the validation of a new bubble 3D reconstruction algorithm in the scope of studying bubble dynamics in a quiescent fluid and at a very low cost (two perpendicular high-speed cameras).

If the experimentation and numerical implementation were two very interesting aspects, I had not the time to study deeply the physics of such flows. I got some insights through my literature review but I remained unaware of several aspects of these flows, of their stakes and their applications. I met various numerical studies involving methods such as the VOF method, which were unknown to me but raised my interest.

The circle is complete through this internship where I considerably strengthened my knowledge of basic CFD while opening a door on multiphase-flow simulations and DNS. It aroused my curiosity even more and I would be delighted to participate, in the future, in the development and applications of such concepts.

I have developed my knowledge on many other aspects such as simulations on clusters, numerical methods and more generally computer tools such as git or python.

Concerning acknowledgements, I would first like to thank my internship supervisor, Guillaume Bois, for his support through the project and his strong expertise. I also need to thank him for his attentiveness and the trust he gave to me.

I am also grateful to Aymeric Sonolet, a PhD student I worked with, for his ability to share his knowledge and give precious advice.

I wish to thank Gabriel Ramirez, a PhD student with whom I shared the office during the first few months of my internship and keep a friendly contact during the lockdown.

Many thanks to the other interns (now freshly PhD students), Clement and Andrew, for the interesting discussions and laughs during coffee breaks. This also applies to other PhDs, Nicolas and Raksmay, and any interns or postdoctoral students that I may have forgotten to cite.

Finally, I feel thankful the laboratory staff, especially Nicolas Dorville, the laboratory head for his introduction to the problematics answered by the CEA and for every contributor I met during the welcome training.

If remote working was tough and full of surprises, Guillaume and other interns were really helpful. It was really important to keep some good working conditions and I am grateful for them.

Contents

Declaration	i
Acknowledgements	iii
List of Figures	viii
List of Tables	ix
1 CEA essence and laboratory overview	1
1.1 Company overview	1
1.1.1 Fields of research and strategic position	1
1.1.2 Paris-Saclay centre	2
1.1.3 International policy	2
1.1.4 Nuclear safety and regulation	2
1.2 Laboratory and unit presentation	3
1.2.1 Hierarchy based on the field of study	3
1.2.2 STMF unit	3
1.2.3 LMSF objectives	3
2 Introduction to internship problematics	4
3 Literature review	6
3.1 Overview of the numerical methods to simulate multiphase flows	6
3.2 Implementation assessment of thermal effects in bubbly and particle flows	6
3.2.1 Validation of diffusion using analytical based model	6
3.2.2 Validation convection using correlations and predictions in a wide range of Reynolds numbers	8
4 Methodology	15
4.1 TrioIJK: from governing equations to numerical methods insight	15
4.1.1 One-fluid formulation of the Navier-Stokes equations	15
4.1.2 One-fluid approach for the temperature equation	17
4.1.3 Discretisation of the one-fluid terms	18
4.2 Temperature equation implementation and validation	18
4.2.1 Validation of the diffusion on a fixed spherical bubble in a quasi-infinite domain and quiescent liquid	18
4.2.2 Convection validation: rise of a spherical bubble	20
5 Results and discussions	25
5.1 Thermal algorithm implementation and accuracy assessment	25

5.1.1	Diffusion validation: a fixed spherical bubble in a quasi-infinite domain	25
5.1.2	Convection validation: rising of a spherical bubble in a tri-periodic domain	29
6	Conclusions	33
	Bibliography	38
A	Overview of the numerical methods to simulate multiphase flows	39
A.1	Lagrangian and Eulerian-Lagrangian: interface tracking inherent methods	39
A.2	Eulerian fluid flow combined with interface tracking	40
A.3	Eulerian fluid flow combined with interface capturing	41
B	Volume of Fluid (VOF) and Front-Tracking (FT) combination in TrioIJK	43
C	Two-fluid (Euler-Euler) model based on time average	44
C.1	Reynolds averaging in the case of single-phase flow	44
C.2	Phase averaging	45
D	Thermal conductivity coefficients in normal and tangential directions to the interface	47
E	ρCp justification during discretisation	50
E.1	Investigation of the use of an arithmetic ρCp calculation	50
E.1.1	Error brought by an arithmetic ρCp calculation	50
E.1.2	Simplified 1D case	50
E.1.3	Solution with a "tweaked" initialisation and an arithmetic ρCp calculation	51
E.2	Justification to the harmonic ρCp calculation	52
F	Supplementary Nusselt number values over time	54
G	Additional observation: solid body rotation to investigate advection scheme positivity	56

List of Figures

Figure 1.1:	Location of the research centres spreaded in France for both Civil (Red) and Military (Blue) applications	2
Figure 2.1:	Turbulence and fluctuation decomposition in bubble channels and swarms	5
Figure 3.1:	Transient non-dimensionalised radial temperature profiles of a hot sphere kept in a pool of cold continuous phase from [6]: (Left) air in water (Middle) alumina in air (Right) alumina in water for both several mesh refinements (stars) and semi-analytical solution (line)	7
Figure 3.2:	Left: Analytical (solid line) versus numerical (symbols) Nusselt number. Right: Mean relative error $\overline{(Nu_{sim}(t) - Nu(t))/Nu(t)}$ depending on the number of elements per diameter N_d from [7]	8
Figure 3.3:	(a) Local Sherwood number around a spherical bubble at every angle (bubble top at $\theta = 0$): Potential solution [25] (Line), $Pe = 300$ (\times), $Pe = 10,000$ (\square) (b) Comparison with the literature of the global Sherwood number for a spherical bubble at several Reynolds numbers (legend in table 3.1)	11
Figure 3.4:	(a) Comparison of the Nusselt number between literature correlations and Euzenat' results [38] (b) More complex configuration: three in-line particles (c) Local Nusselt numbers on each sphere	14
Figure 4.1:	Modified 1D finite-difference formulation of the problem being inspired by Das et al. [5]	18
Figure 4.2:	(a) Schematic of the simulated configuration: a viscous and spherical fixed bubble mimicking a rising bubble, (b) Nusselt number correlation for a liquid Prandtl number $Pr = 1$ [37]	21
Figure 5.1:	Effect of the mean λ calculation on the solution ($\alpha_{vap}/\alpha_{liq} \approx 200$). 1D-FD represents the reference solution. (a) Arithmetic $\lambda_a = \sum_k \lambda_k I_k^c$, (b) Harmonic $\frac{1}{\lambda_h} = \sum_k \frac{I_k^c}{\lambda_k}$ with $I_k^c = \frac{\int_{V_c} \chi_k dV}{V_c}$	25
Figure 5.2:	Effect of the ρCp calculation on the solution ($\alpha_{vap}/\alpha_{liq} \approx 200$): (a) Arithmetic $\frac{1}{(\rho Cp)_a} = \frac{1}{\sum_k \rho_k C_p k I_k^c}$, (b) Harmonic $\left(\frac{1}{\rho Cp} \right)_h = \sum_k \frac{I_k^c}{\rho_k C_p k}$ with $I_k^c = \frac{\int_{V_c} \chi_k dV}{V_c}$	27
Figure 5.3:	For $1/\lambda_h = \sum_k I_k^c / \lambda_k$ and $(1/\rho Cp)_h = \sum_k I_k^c / (\rho_k C_p k)$ with $I_k^c = \int_{V_c} \chi_k dV / V_c$ (a) Air-Water, (b) Alumina-Air, (c) Alumina-Water	28
Figure 5.4:	(a) Nusselt number over time for $Re(\mu_v/\mu_l = 0.1) = 344$ and $Re(\mu_v/\mu_l = 1) = 320$, $Pr_l = [1; 2.62]$ and $\mu_v/\mu_l = [0.104; 1]$ (b) Average Nusselt number values depending on the Reynolds number	29

Figure 5.5:	(a) Nusselt number over time without diffusion for $Re(\mu_v/\mu_l = 0.1) = 344$ and $Re(\mu_v/\mu_l = 1) = 320$, $Pr_l = [1; 2.62]$ and $\mu_v/\mu_l = [0.104; 1]$ (b) Corrected Nusselt number values depending on the Reynolds number (c) Nusselt number values from spurious temperature leakages in pure advection and for various spatial resolution	30
Figure 5.6:	Liquid Nusselt number convergence for a set of three mesh resolutions at $Re(\mu_v/\mu_l = 0.1) = 344$ (a) $Pr_l = 1$, (b) $Pr_l = 2.6$. (c) Both Prandtl numbers The resolution is in number of elements per diameter	31
Figure 5.7:	Vapour and liquid Nusselt number Nu_v and Nu_l at $Re(\mu_v/\mu_l = 0.1, Pr_l = 1) = 344$ for a resolution of 25 (a) and 35 (b) elements per diameter. (c) Nu_v to Nu_l at $Re(\mu_v/\mu_l = 0.1) = 344$ and for various resolution and liquid Prandtl number	32
Figure A.1:	Front tracking method from Tryggvason [1]: (a) Interface discretisation, (b) Elements rebalancing	40
Figure A.2:	Nakayama volume tracking method [46]	40
Figure A.3:	(a) Fluid fraction to locate the bubble and its boundary inside the domain, (b) Original interface reconstructed using the SLIC, the Hurt and Nichols and the PLIC methods b,c and d, respectively	41
Figure A.4:	Signed distance function used to represents the phase: the zero level-set corresponds to the interface. Coalescence and break-up can be modelled implicitly	42
Figure D.1:	Heat flux conservation in the normal direction \mathbf{n}	47
Figure D.2:	Heat conservation in the tangential direction \mathbf{t}	48
Figure E.1:	Mixed cell with 1D flux $q = q_v = q_l$	51
Figure E.2:	Solution using a "tweaked initialisation" for $1/\lambda_h = \sum_k I_k^c / \lambda_k$ and $1/(\rho Cp)_a = \sum_k I_k^c / (\rho_k C p_k)$ with $I_k^c = \int_{V_c} \chi_k \, dV / V_c$ (a) Air-Water, (b) Alumina-Air , (c) Alumina-Water	51
Figure E.3:	Decomposition of the flux	52
Figure F.1:	Nusselt number over time for various Reynolds numbers, viscosity ratios and liquid Prandtl numbers	55
Figure G.1:	Temperature values out of the bounds over time depending on the Courant number (CFL)	57
Figure G.2:	Temperature distribution at the beggining and at the end of the simulation for $CFL = 0.25$: (a) 16 elements per diameter, (b) 32 elements per diameter	58

List of Tables

Table 3.1:	Data and correlations from several authors used in the validation process	12
Table 4.1:	Phase and domain properties	20
Table 4.2:	Summary of parameters tested. The velocity V_{term} in the definition of Re_b is estimated based on the correlation. The actual Re_b obtained in the simulation will be slightly different	23

Chapter 1

CEA essence and laboratory overview

Note: All the information concerning the company has been provided orally throughout a welcome training with several supervisors (laboratory, unit, safety manager...) and through the CEA website.

1.1 Company overview

Originally, the French Alternative Energies and Atomic Energy Commission also referred to as CEA was created to undertake researches to make the most of scientific, industrial, and military potential of atomic energy. Later they have diversified their activities and developed strong expertise in many fundamental and industrial fields. Nowadays, the CEA is still confirming its competences in nuclear research while answering new challenges such as in low carbon energy alternatives or the science of matter and universe.

1.1.1 Fields of research and strategic position

The CEA is a French public research leader answering sciences, technical and industrial problematics. It is focusing on four main topics:

- Security and defence where the nuclear deterrence and surveillance are defined as guiding principles.
- Low-carbon energies such as nuclear and renewable energies where it acts proposing innovative solutions for energy production, conversion, storage, resources or material life cycle. The global stake is to converge to different energy scenarios answering techno-economic issues. The demand concerning the reduction of nuclear usage has inevitably widened the research spectrum.
- Technological research for the industry where it stands as an innovation catalyst from small companies to bigger groups by leading projects between level 3 and 7 of the Technology Readiness Level (TRL). The CEA LETI, specialised in nano-electronics or computer vision has contributed to many innovations that have been promoted to the commercial market. Consequently, it provides solutions in many realisable and marketable technologies working hand in hand with industries by answering their needs.
- Fundamental research i.e. in physical and life sciences throughout interdisciplinary projects in biology, chemistry, nano-technologies and sciences, physics or health. For example, they highly contribute to develop and make use of instrumentation for LHC (CERN, Switzerland) or Herschel spatial telescope.

The CEA is involved in many European projects while its international presence is in constant improvement. The great reputation of the CEA is mainly due on its wide and rich field of expertise shared throughout several collaborative projects with both academy and industry.

Split into nine centres, located across strategical places in France (see Fig.1.1), the CEA can create local partnerships. Its large involvement in the state of the art technologies and research allows its sitting as a major stakeholder at different organisations and alliances. As an example, CEA is attending

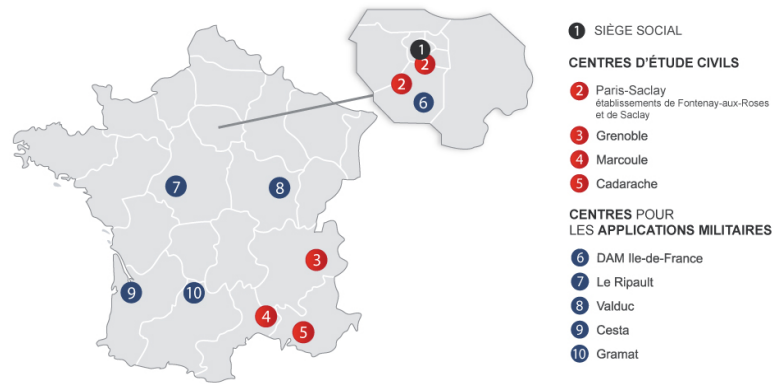


Figure 1.1: Location of the research centres spreaded in France for both Civil (Red) and Military (Blue) applications

the French research in energy (ANCRE) or also the ALLISTENE, standing for digital science and technology. In 2019, the CEA appeared to be the 1st organisation in terms of numbers of patents registered in Europe.

If CEA was established in 1945 with the scope of developing a deep knowledge of the matter and atoms, its fields of research became rapidly multiple to answer indirect problems such as in material sciences or microelectronics (simulations and measurements). Atomic research requires complex and specific tools which are not directly available technologies. The multi-disciplinary aspect of these studies is inevitable and general improvement of atomic research is achieved through those of the surrounding technologies.

1.1.2 Paris-Saclay centre

Gathering more than 7,000 researchers, the centre of Paris-Saclay is involved in a wide range of activities underlined previously such as matter sciences, low-carbon energy, health or technological research. It is also part of the University of Paris-Saclay community, representing 15% of the national research.

1.1.3 International policy

The CEA is participating in sovereign missions and acts as a nuclear advisor for the French government. Thanks to its deep knowledge, the CEA can contribute to policies elaboration: from foreign nuclear policy and international cooperation to sensible technologies protection and control through environmental and energy strategies.

CEA is not only supporting the french nuclear industry. It gives also advice and it assists the foreign countries that wish to undertake a nuclear power plant establishment project. International french nuclear agency (AFNI) is providing these consulting services through a company such as the CEA, the ANDRA (specialised in nuclear waste management) or the national agency of nuclear safety and radio-protection (IRSN).

1.1.4 Nuclear safety and regulation

The Atomic Energy Commission is in charge of developing nuclear state of the art technologies involved naturally in the exploitation of the nuclear power plants. Moreover, the experimental research is dependant on nuclear installations and their continuous observation over time.

It leads the CEA to make environmental issues and people safety a key priority. Academic reactors as well as the treatment centres of radioactive wastes are thus exploited in a way to answer new chal-

lenges and preoccupations. Other risks such as chemical or laser risks are also investigated throughout several specific programs.

Nuclear installations are also controlled by external organisms *i.e.* the Safety Nuclear Authority (ASN) and the Safety Nuclear Defense Authority (ASND) in charge of the civil and military installations, respectively.

1.2 Laboratory and unit presentation

1.2.1 Hierarchy based on the field of study

The research at CEA is divided into several departments depending on their scope and field of study. The department is subdivided into several units and then into laboratories.

Each organism is constantly sharing their work internally and the laboratories work jointly throughout projects for a common goal: the up-scaling approach *i.e.* from a local scale, to understand deeply particular flows, to overall nuclear plant physics via precise component modelling.

1.2.2 STMF unit

STMF acronym stands for thermo-hydraulic and fluid mechanics unit and is part of the structures and system department (DM2S). It is composed of six laboratories working on the previously cited up-scaling approach. Some laboratories are focusing on experimentation (LIEFT) while others are specialised in software development (LGLS). Other are working on different scales: reactor, component or local for the LMES, LMEC and LMSF laboratories, respectively. The last lab is dedicated to applications (LATF).

1.2.3 LMSF objectives

The laboratory of fluid mechanics and simulation (LMSF) shows several fields of interest. The laboratory is developing its own fluid dynamics software named TrioCFD to perform multi-scale and massive parallel calculations. The range of applications is wide: from safety reactor analysis at the global scale to more fundamental research focusing on particular flow configurations at the local scale.

The increasing computational power allows the research to be focused on the refinement and optimisation of large scale and averaged simulations from local numerical studies performed by Direct Numerical Simulations (DNS) in some two-phase conditions or Large Eddy Simulations (LES) in other configurations. It allows also studying deeply certain types of flows to strengthen scientific knowledge. The current platform derived from TrioCFD and used to perform DNS over bubbly flows during my internship is named TrioIJK and is dealing with cartesian and structured meshes only.

Chapter 2

Introduction to internship problematics

Recent work of the laboratory has been carried out on bubbles rising in channels or bubble swarms for both numerically fixed or free bubbles configurations. Through the work of a PhD student, these turbulent bubbly flows were studied numerically using direct numerical simulations (DNS) applied on the Navier-Stokes one-fluid formulation [1] combined with the volume of fluid (VOF) and front tracking methods for the inter-facial treatment.

This study was made in the scope to characterise more precisely velocity fluctuations in such flows. DNS allows capturing the turbulence of the fluid at the Kolmogorov scale while the averaged Navier-Stokes equations (RANS) use commonly turbulence models such as $k - \varepsilon$ to take into account the time-averaged instantaneous fluctuations. In the case of multiphase flows, two-fluid models are used instead. The inter-phase interactions are modelled in the form of empirical correlations that could be used as in Panicker's paper [2]. However, no model deduced from post-processed averaged values of instantaneous fluctuations in swarms is available in the literature.

RANS simulations are preferable to simulate large scale configurations (reactors, industrial processes) because of their reasonable computational cost but need models to take into account the small scale not captured during the simulations. Experimental data is sometimes not handy to obtain to establish these models, that is why the growing use of DNS is justified. The statistical post-processing of these local simulations is then used to this purpose. Models can be established based on periodic configurations, and easily reused in more general simulations. It is particularly suited for bubbly flows, as large and complex bubble configurations could be simplified to the smaller random configuration of bubbles, studied over time.

It is thus essential to characterise precisely the fluctuations induced by the bubble referred sometimes crudely to as turbulence. Several studies were made to decompose these fluctuations into several contributions whether it is due to the bubble wake, the wall effect or the form of a potential flow (see Fig.2.1 by du Cluzeau, Bois and Toutant [3]). However, all the publications are not reaching a consensus. Depending on the void fraction, the flow may be homogeneous or inhomogeneous which has led to different observations and decomposition proposals. The laboratory is focusing on expanding their knowledge on the interactions between the different fluctuation components while unifying the different observations depending on the flow conditions.

The laboratory has been working on the modelling of the vapour-liquid phase dynamic interactions in swarms and channels. However, they have not studied the heat transfer between the two phases yet.

With the same approach, Aymeric Sonolet, a PhD student, is currently working on this problematic. His goal is to simulate heat transfer in heated wall channels and tri-periodic swarms to post-process averaged thermal fluctuations. The post-processing of the data using machine learning algorithms will potentially allow establishing correlations to close a two-fluid model (Euler-Euler). However, such models are generally valid in a certain range of void fraction, Reynolds number, Prandtl number and other physical parameters. For the laboratory, the goal is to obtain a sufficiently large spectrum to

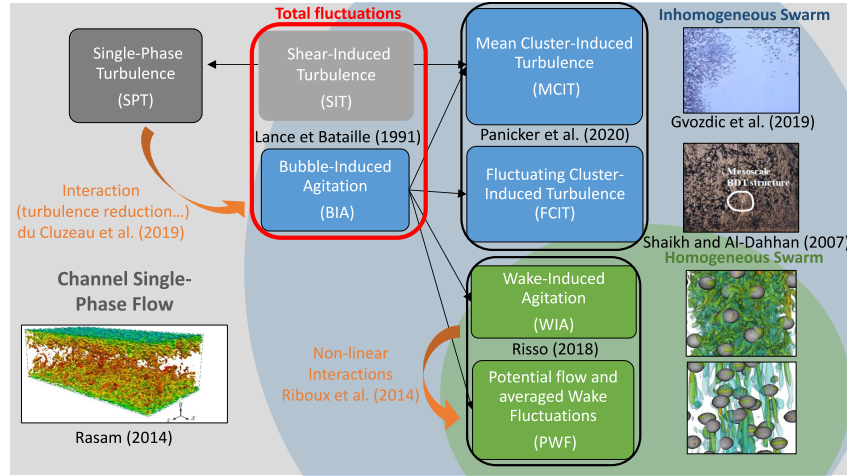


Figure 2.1: Turbulence and fluctuation decomposition in bubble channels and swarms

develop its knowledge while keeping a link with the phenomenon observed in nuclear applications and experimental data available.

My work consisted mainly in assisting Aymeric in his work by validating its energy equation implementation in both pure diffusion and convection before running more complex simulations. The aim was to ensure the validity of the results with sufficient tests while checking the various approximations made during the discretisation of the equation due to the complexity of its implementation (in particular in regards of inter-facial discontinuities and transfers).

Many approaches are available to study multiphase and bubbly flows. A quick review has been written to contextualise the methods implemented in TrioIJK, the current simulation code developed by the laboratory. Then, a review of various heat transfer correlations raising our interest to validate the simulations will be presented. Some papers involving benchmarks of growing complexity will be introduced. According to their different strategies and our current time and code limitations such as boundary conditions, an approach is later established and presented.

Chapter 3

Literature review

3.1 Overview of the numerical methods to simulate multiphase flows

A quick overview of various numerical methods involved in multiphase flows simulations is presented in appendix A. It is not essential to the understanding of the following work but gives a general insight into the pros and cons of the methods used in the current software TrioIJK.

3.2 Implementation assessment of thermal effects in bubbly and particle flows

A model implementation validation is essential in multi-physics problems. They are indeed established in the scope of solving complex and coupled situations where dynamics effects can interact with thermal ones. As a consequence, the implementation of both parts should be first investigated separately.

In our case, the implementation of the flow dynamics has been covered earlier through the laboratory research and its associated PhD work [4]. On the contrary, the temperature equation has been recently added to the original simulation code to undertake studies on heat transfer over bubble swarms (periodic boundaries) or bubbly flows in wall-heated channels.

Several benchmarks are commonly used to test particle flows or bubbly flows depending on the model we try to implement *i.e.* with or without phase change. The first step for the laboratory is to implement the thermal effects without phase change. It is done as it is less complex but also to consider a precise void fraction and bubbles diameter representing a desired type of flow to study. It is also much more convenient for periodic configurations.

Thermal effects assessment can be split between diffusion and convection, allowing to test growing complexity situations. A special focus is set upon inter-facial transfers.

3.2.1 Validation of diffusion using analytical based model

Das *et al.* [5] have investigated a sharp-interface Immersed Boundary Method to simulate heat transfer. To test the implementation of their heat transfer algorithm over a spherical bubble Das *et al.* [5] have chosen to solve a uniaxial diffusion equation (radial axis in spherical coordinates) using finite difference.

By initialising a temperature difference between the two phases, the domain temperature can be predicted over time. This 1D Finite difference simulation is converging fast, at very low cost and provides thus a good way to assess the temperature convergence of a more complex 3D model like ours. Panda *et al.* [6] used efficiently this method to check their diffusion algorithm using three combinations of gas/liquid, solid/gas and solid/liquid providing a large range of results depending on the thermo-physical properties jump as shown in Fig.3.1. This method aims to check the temperature error locally over the domain. An asymptotic integral value such as a Nusselt Number can not be deduced in such case of diffusion. We implemented the one-dimensional resolution of the problem using finite differences as shown later and used the results as a reference to compare to TrioIJK simulations.

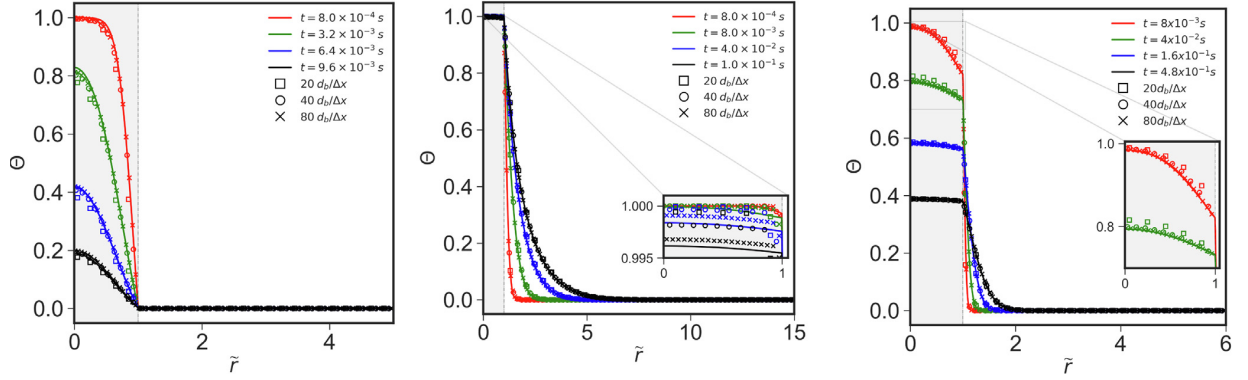


Figure 3.1: Transient non-dimensionalised radial temperature profiles of a hot sphere kept in a pool of cold continuous phase from [6]: (Left) air in water (Middle) alumina in air (Right) alumina in water for both several mesh refinements (stars) and semi-analytical solution (line)

Nusselt number limitation could be overcome enforcing a high heat capacity and a high diffusivity in the bubble to keep a constant temperature inside the bubble. If it is done during a sufficiently long time it could be possible to obtain an asymptotic-like value of Nusselt close to the limiting value of 2. It is finally not worth in this case as the convection test will be more demanding.

Thiam *et al.* [7] went further trying to compare the Nusselt number $Nu = h_{liq}d_{sphere}/\lambda_{liq}$ modelling the heat transfer from a solid spherical particle at constant temperature to the fluid domain. From an analytical calculation of the temperature based on the vicinity of the sphere, an associated Nusselt number over time can be developed:

$$Nu(t) = 2 + \frac{d_{sphere}}{\sqrt{\pi\alpha_{liq}t}} = 2 + \frac{1}{\sqrt{t^*}} \quad (3.1)$$

where α_{liq} denotes the fluid diffusivity. The simulated Nusselt can be found through the heat transfer coefficient h_{liq} expressed from the liquid temperature gradient at the interface ∇T_{liq} or from an inlet-outlet energy balance as follows (Eq. 3.2):

$$Q_{sphere \rightarrow liq} = h_{liq}A(T_S - T_\infty) = \int_{S_{sphere}} -\lambda_{liq}\nabla T_{liq} \cdot \mathbf{n}dS \quad (3.2)$$

where T_S is the sphere surface temperature and T_∞ is the temperature of the infinite flow-field.

Analytical and simulated Nusselt numbers can thus be compared over time while the rate of convergence could be observed depending on the number of elements as shown in figure 3.2. This method has only a physical meaning when the particle has a sufficiently high conductivity to keep an homogeneous temperature.

In the presence of phase change, the Scriven solution [8] is a good way to validate both diffusion and bubble growth like in Tanguy *et al.* paper [9].

In spherical coordinates, the energy equation can be expressed depending on the bubble radius $R(t)$ as follows (Eq.3.3):

$$\frac{\partial T}{\partial t} + \varepsilon \frac{\dot{R}(t)R^2(t)}{r^2} \frac{\partial T}{\partial r} = \alpha \left(\frac{\partial^2 T}{\partial r^2} + \frac{2}{r} \frac{\partial T}{\partial r} \right) \quad (3.3)$$

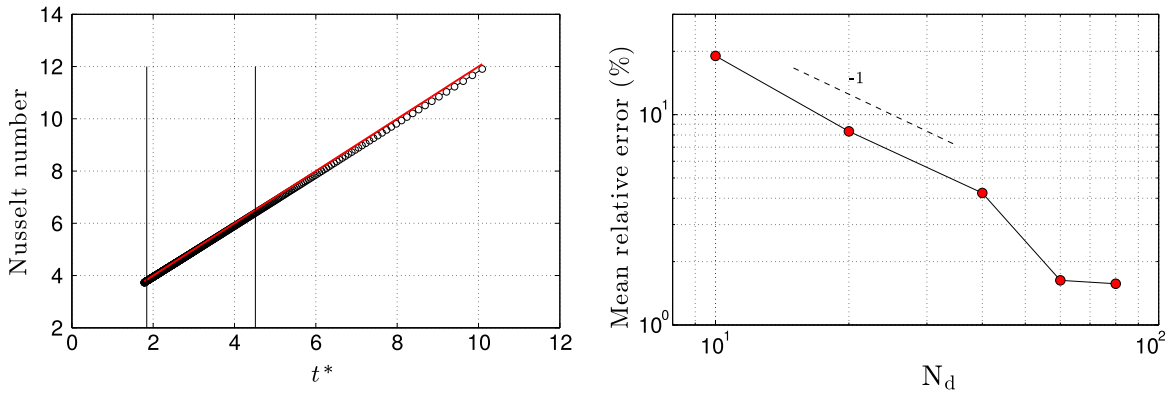


Figure 3.2: Left: Analytical (solid line) versus numerical (symbols) Nusselt number.

Right: Mean relative error $\overline{(Nu_{sim}(t) - Nu(t))}/Nu(t)$ depending on the number of elements per diameter N_d from [7]

Where $\varepsilon = \left(1 - \frac{\rho_{vap}}{\rho_{liq}}\right)$, $R(t) = \beta\sqrt{\alpha t}$ and β represents its unknown growth rate. Using the Jakob number (Ja), defined as the ratio of the sensible heat to the heat released during the phase change, Tanguy *et al.* [9] developed an iterative resolution from equation 3.4.

$$Ja = \frac{\rho_{liq} C p_{liq} (T_\infty - T_{sat})}{\rho_{vap} L_v} = 2\beta^3 \exp(\beta^2 + 2\varepsilon\beta^2) \int_{+\infty}^{\beta} \frac{\exp\left(-x^2 - \frac{2\varepsilon\beta^3}{x}\right)}{x^2} dx \quad (3.4)$$

where L_v is the latent heat of vaporisation. This implicit equation can be solved iteratively by updating the growth rate β until satisfying the Jacob number (Ja).

In conclusion, diffusion can not be checked by the same approach depending on the assumptions made. A transient and steady-state configuration could be analytically found for a solid particle with high conductivity (constant temperature assumed) while semi-analytical transient solutions can only be found for bubbles in real physical conditions. A global value characterising the heat transfer such as a Nusselt number or a Jakob number makes only sense in the case of a sphere at constant temperature *i.e.* for a solid particle or in the presence of phase change. For transient solutions and no phase change, like in our case, we can only perform a temporal study of temperature.

3.2.2 Validation convection using correlations and predictions in a wide range of Reynolds numbers

Various solutions for Nusselt numbers can be found in the literature over wide ranges of Reynolds numbers. Particular attention needs to be given to the assumptions made to obtain these solutions. Depending on the nature of the sphere lying in the flow (an inviscid bubble, a viscous one or a solid particle), the dynamic of the flow and consequently the heat transfer will be different. The ratio of viscosities λ between the sphere and the surrounding fluid is then a key parameter and it takes more importance at higher Reynolds numbers.

Analytical solutions for viscous bubbles and solid spheres in Stokes flows ($Re < 1$)

To study convection, some definitions need to be introduced. For heat transfer, the Peclet number is an essential non-dimensionalised variable that is defined depending on the Reynolds number and the

Prandtl number (Pr) (or the Schmidt number (Sc), i.e. its equivalent in mass transfer). The Peclet number is the product of the two latter terms, hence, $Pe = Re\text{Pr} \equiv Re\text{Sc}$ (mass) .

Checking the convection is less handy. Indeed, analytical solutions for the convection-diffusion equation for bubbles and particles can rarely be found except for simple configurations. It is especially the case at very low Reynolds numbers $Re \ll 1$ and small but finite Peclet numbers i.e. the ratio of advective transport rate over the diffusive one such as $Pe = Lu/D$ (where L is the characteristic length such as the bubble diameter, u the relative velocity and D the thermal or mass diffusivity of the liquid).

For such state of motions, referred to as creeping or Stokes flows, it can also be shown that the Nusselt number Nu becomes a function of the Peclet number for a given viscosity ratio like for solid spheres or inviscid bubbles. Similarly to Hadamard [10] who derived an analytical solution for sphere motion using a stream function for $Re \ll 1$, several asymptotical solutions for the Nusselt number have been found at low Reynolds (still $Re \ll 1$) but fixed Peclet numbers [11–15]. High Prandtl numbers occur in many industrial or organic applications so these extensions to Hadamard solution may raise more interest in real applications.

However, the existence of this type of solution is based on assumptions concerning the temperature field. Kronig *et al.* [11] derived their solution assuming a sufficiently large coefficient of heat conduction in the sphere compared to the surrounding medium so that the sphere is kept at a uniform temperature. It leads to equation 3.5.

$$Nu = 2 + \frac{1}{2}Pe + \frac{581}{1920}Pe^2 + O(Pe^3) \quad (3.5)$$

This equation over an isothermal sphere was corrected later by Acrivos *et al.* and Leal *et al.* [12–14], [15] respectively (see Eq.3.6). If the assumptions were the same, they used a different expansion of the convection equation.

$$Nu = 2 + \frac{1}{2}Pe + \frac{1}{4}Pe^2 \ln \frac{Pe}{2} + 0.2073Pe^2 + \frac{1}{16}Pe^3 \ln \frac{Pe}{2} \quad (3.6)$$

All the previous analytical solutions were found around solid spheres i.e. when the viscosity ratio denoted $\lambda = \mu_{\text{sphere}}/\mu_{\text{surrounding-fluid}}$ tends towards infinity. Michaelides [16] and Levich [17] raised an important practical fact about bubbles. The conditions of purity (in the case where $\lambda \rightarrow 0$) at a bubble surface is rarely verified as some surfactant or impurities are usually abundant in industrial processes. It affects bubble behaviour and physics in such a way that viscous spheres are often closer to solid ones. That is why all the previous theory can still find some applications in heat transfers in bubbly flows at low Reynolds numbers.

However, Levich [17] derived an expression of the Nusselt depending on the viscosity ratio for viscous spheres. Their expression is valid for $Re \ll 1$ and $Pe \gg 1$:

$$Nu = \sqrt{\frac{4Pe}{3\pi(1+\lambda)}} \quad (3.7)$$

At similar steady conditions and Reynolds number magnitude, Michaelides obtained more accurate results from a numerical study for $Pe > 1$. Same author derived also a supplementary correlation for low but finite Reynolds numbers $Re < 1$. They finally got a correlation depending on λ as follows:

$$Nu = 1.49Pe^{0.322+} \frac{0.113}{0.361\lambda + 1} \quad (3.8)$$

The use of the previously cited analytical and asymptotic solutions is restrained to a very small range of Peclet numbers. It has been shown that the correlations are often found using an infinite viscosity ratio (sphere viscosity large enough compared to the surroundings) which corresponds to a solid sphere. In this range of Reynolds numbers, the difference between bubbles and particles is quite low and the fluid field mainly depends on the viscosity of the surrounding fluid. It is noticeable that the Nusselt number is derived from the value of 2. It corresponds to its value in the case of pure diffusion from a sphere at a constant temperature difference from its surrounding.

Creeping flows are often approached using potential flow theory. As the viscous forces are dominating, no detachment occurs in such type of flows so the irrotational condition is verified *defacto*. It becomes less valid for higher Reynolds number configurations until the flow transitions to a fully turbulent state.

Analytical predictions for inviscid bubbles in mid-range Reynolds numbers

Potential flow approaches are also suited for inviscid bubbles and have led to good predictions over a wider range of Reynolds numbers. As there is no shear at the interface, flow separation occurs at higher Reynolds numbers. A boundary layer description is often combined with the potential function to refine the solution. Considering a larger viscosity in the surrounding medium than in the bubble, analytical solutions of the Sherwood number (mass transfer equivalent of the Nusselt number) can be developed.

To do so, Boussinesq [18], Leclair and Hamielec [19] or Winnikow [20] solved the convection-diffusion equation by substituting the velocity by the previously calculated potential flow, the velocity distribution given by Hamielec [21] and the velocity distribution given by moore [22], respectively. Takemura *et al.* [23] corrected these predictions to fit their experimental data, up to a Reynolds number of 100.

It is important to notice that these predictions were realised considering a constant concentration inside the bubble. At the infinity *i.e.* far in the surrounding domain, the concentration was considered to be zero. Also, Takemura underlined one important assumption of all previously cited papers [18–20]: they assumed that the effects of flow inside a bubble on the dissolution process are small. By comparison with the heat transfer, the previous assumption corresponds to a constant temperature inside the bubble which is true in presence of phase change.

Using these predictions as a point of comparison, Legendre *et al.* [24] undertook a general study on convection-diffusion equation for any non-dimensionalised temperature or concentration $\tilde{c} = (c - c_\infty)(c_i - c_\infty)$ *i.e.* valid for both heat and mass transfer (c is dimensional, i denotes the interface). Their work aimed to analyse the effect of the bubble aspect ratio, defined through its major and minor axes, for any of the two latter transfers using DNS.

Legendre and Figueroa-Espinoza dealt with this problem using one type of transfer: the mass one. The Sherwood number $Sh = f(Re, Sc)$ is thus used and its thermal equivalent is the Nusselt number $Nu = f(Re, Pr)$. The Peclet number previously introduced is expressed for both transfer but the diffusivity coefficient is replaced depending on the type of transfer (D_m or α).

Convection-diffusion equation, once dimensionless, is given by equation 3.9 where $Pe = Lv_\infty/D = ReSc \equiv RePr = Lv_\infty/\alpha$.

$$\frac{\partial \tilde{c}}{\partial \tilde{t}} + \nabla \cdot (\tilde{\mathbf{v}}\tilde{c}) = \frac{1}{Pe} \nabla^2 \tilde{c} \quad (3.9)$$

The simulation is thus focusing only on the external fluid domain. At the bubble boundary, the concentration is constantly equal to 1. Considering no slip conditions and a variable η following

the outward bubble normal \mathbf{n} , the boundary conditions, expressed as follows, translate the inviscid characteristic of the bubble (Eq.3.10):

$$\begin{cases} \tilde{\mathbf{v}} \cdot \mathbf{n} = 0 & \text{at } \eta = 0 : \text{No penetration} \\ \mathbf{n} \times (\tilde{\tau} \cdot \mathbf{n}) & \text{at } \eta = 0 : \text{No shear at the interface} \\ \tilde{c} = 1 & \text{at } \eta = 0 : \text{Concentration at the interface} \\ \tilde{c} = 0 & \text{at } \eta = 1 : \text{Concentration far in the domain} \end{cases} \quad (3.10)$$

Effect of the bubble shape on the transfer is expressed through a global Sherwood number (or Nusselt number) shown in equation 3.11:

$$\begin{cases} Sh_{global} = \frac{\int_{A_b} D \nabla c \cdot \mathbf{n} dA_b}{D(c_s - c_\infty) A_b} = \frac{\int_{A_b} Sh_{loc} dA_b}{A_b} \\ Sh_{loc} = L \frac{\nabla c \cdot \mathbf{n}}{c_s - c_\infty} \end{cases} \quad (3.11)$$

Legendre *et al.* achieved their validation procedure using a comparison between the simulated Sherwood number (both local and global) and literature correlations for inviscid bubbles as shown in figures 3.3a and 3.3b.

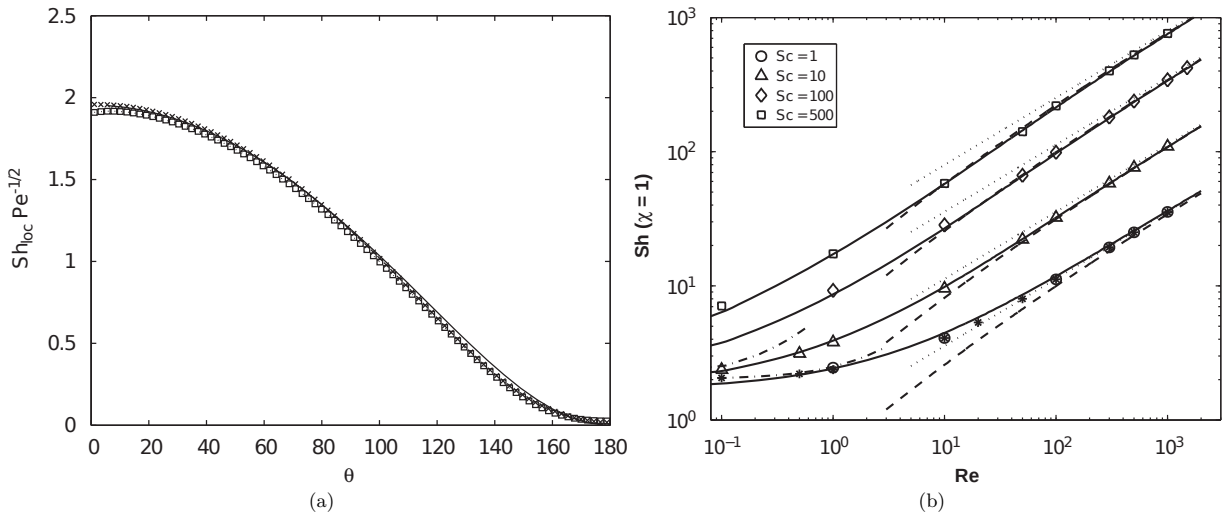


Figure 3.3: (a) Local Sherwood number around a spherical bubble at every angle (bubble top at $\theta = 0$): Potential solution [25] (Line), $Pe = 300$ (\times), $Pe = 10,000$ (\square)
 (b) Comparison with the literature of the global Sherwood number for a spherical bubble at several Reynolds numbers (legend in table 3.1)

On Fig.3.3a, the local Sherwood in the spherical bubble tangential direction is plotted depending on the angle (in the bubble frame of reference) and compared to Favelukis and Ly [25] potential solution for two Peclet numbers $Pe = 300$ and $Pe = 10,000$. Other expressions could have been used such as Boussinesq [18] or Ruckenstein [26] ones.

Finally, the global Sherwood is compared to multiple predictions and correlations depending on the Reynolds range [18, 20, 23, 27, 28]. Legend is shown in the table 3.1.

Results of Legendre *et al.* [24] in the case where $Re = 300$ and $Sc = 500$, showed a relative difference from only 1.5% up to 8% according to Takemura *et al.* and Boussinesq's values respectively. Winnikow's

Table 3.1: Data and correlations from several authors used in the validation process

Marker or line type	Authors	Data type
*	Legendre and Magnaudet (1999) [27] using a different grid	Numerical
--	Takemura and Yabe (1998) [23]	$Sh^{TY} = \frac{2}{\sqrt{\pi}} \left[1 - \frac{2}{3} \frac{1}{(1 + 0.09Re_{eq}^{2/3})^{3/4}} \right]^{1/2} (2.5 + Pe_{eq}^{1/2})$
--	Winnikow (1967) [20]	$Sh^W = \frac{2}{\sqrt{\pi}} \left[1 - \frac{2.89}{\sqrt{Re_{eq}}} \right]^{1/2} Pe^{1/2}$
...	Boussinesq (1905) [18]	$Sh^B = \frac{2}{\sqrt{\pi}} Pe^{1/2}$
- - - -	Kronig <i>et al.</i> (1951, thermal) [11] or Brenner (1963, mass) [28]	$Sh^{Bre} = 2 + \frac{Pe}{2}$

correlation is also in very good agreement with computed results up to 1% for the previously cited case.

The range of relative difference is relatively narrow around the numerical DNS values. For low Reynolds cases, Brenner's correlation seems also in good agreement while Takemura's one is not converging well when Re or Pe tends towards zero.

Their results for different aspect ratios could eventually be used as a further benchmark but may be heavy.

In conclusion, the validation of Legendre and Figueroa has been realised on spherical bubbles at mid-range Reynolds numbers which is a relevant approach for our study. However, our simulations do not involve inviscid bubbles. Moreover, the capacity of the VOF formulation to handle high property jumps such as viscosity is not ideal. Ensuring convergence and being in good agreement with the theory is thus risky using this inviscid bubble approach with our code and not particularly representative of our needs. Still, it is a good reference to answer our need in terms of methodology and is used for validation of the convection-diffusion case in section 4.2.2.

Correlations for fully turbulent flows at various viscosity ratios

For higher Reynolds numbers involving recirculation zones, hence where the potential flow approach is no longer valid (rotational flow), a diversity of Nusselt number correlations from experiments [16, 29–31] could be used as a further approach in the case of a solid particle.

Immerging a solid particle with constant temperature in a sufficiently large domain and applying an inlet velocity field to mimic a rising (or falling) particle could be a first step to validate a simulated model. The Nusselt number can be computed from the heat balance between the inlet and outlet of the domain and compared to Nusselt number correlations such as the one of Feng and Michaelides [16].

$$Nu = 0.992 + Pe^{1/3} + 0.1Pe^{1/3}Re^{1/3} \quad 0.1 \leq Re \leq 4000 \quad 0.2 \leq Pe \leq 2000 \quad (3.12)$$

To mimic such type of benchmark for a bubble, imposing a high surface tension to keep a spherical shape, a high bubble viscosity and a high diffusion coefficient to keep a uniform bubble temperature over time is worth considering.

But once again it is not interesting for us to enforce a high viscosity inside the bubble to mimic a solid particle as the finality of the code is to simulate a bubbly flow of saturated water at around 100 bar *i.e.* where the viscosity ratio is far from infinity. Using the current boundary condition and applying a quasi-infinite viscosity jump may not be supported by the algorithm as highlighted previously.

From the Harper and Moore asymptotic velocity solution [32], Weber [33] proposed in 1975, one correlation depending on the Reynolds number and the viscosity ratio λ for density ratios $\rho_{sphere}/\rho_{fluid}$

in the range $[0; 4]$ only (Eq.3.13). Multiple correlations were later available in the literature [34],[35] but are only valid in a narrow range of parameters.

$$Nu = \frac{2\sqrt{Pe}}{\sqrt{\pi}} [1 - Re^{-1/2} (2.89 + 2.15\lambda^{0.64})]^{1/2} \quad \lambda \leq 2 \quad 0 \leq \rho_{sphere}/\rho_{fluid} \leq 4 \quad (3.13)$$

For example, the solution derived by Clift *et al.* [35] using Hamieliec's velocity results [36] is only valid for intermediate Reynolds numbers (Re around 200).

More recently, Feng and Michaelides [16, 37] performed a numerical study and established two correlations in both ranges of viscosity ratio $\lambda \in [0; 2]$ and $\lambda \in]2; \infty[$. They solved Steady Navier-Stokes and energy equations combined with a two sub-layers concept to describe the flow distribution close and far from the interface. However, this heavy correlation is only valid for Peclet number from 10 up to 1000. Assuming an average Reynolds number of 400 in our swarm simulations, it allows Prandtl numbers up to 2.5, which seems to be the best alternative, at least for validation purposes.

$$\left\{ \begin{array}{l} Nu(Pe, Re, 0 < \lambda < 2) = \frac{2-\lambda}{2} Nu(Pe, Re, 0) + \frac{4\lambda}{6+\lambda} Nu(Pe, Re, 2) \\ Nu(Pe, Re, 2 \leq \lambda) = \frac{4}{2+\lambda} Nu(Pe, Re, 2) + \frac{\lambda-2}{\lambda+2} Nu(Pe, Re, 2) \\ Nu(Pe, Re, 0) = 0.651Pe^{1/2} \left(1.032 + \frac{0.61Re}{Re+21} \right) + \left(1.60 - \frac{0.61Re}{Re+21} \right) \\ Nu(Pe, Re, 2) = 1.41 + 0.64Pe^{0.43} (1 + 0.233Re^{0.287}) - 0.15Re^{0.287} \\ Nu(Pe, Re, \infty) = 1.3 + 0.852Pe^{1/3} (1 + .0233Re^{0.287}) - 0.182Re^{0.355} \end{array} \right. \quad (3.14)$$

Growing complexity validations

As underlined by Euzenat [38] in his thesis on heat transfer in dense free particles beds, grid convergence tests [39],[40] using Nusselt number profiles over simplified configuration is not representative of more complex flows. It gives the first level of information that could be enhanced simulating configurations with growing complexity.

Euzenat [38] started its validation similarly to Thiam *et al.* [7] using a fixed particle in both quiescent and moving fluid *i.e.* from purely diffusive to strongly convective flow (see Fig.3.4.a). But he went one step further using a more complex configuration. Three particles were initialised along the main axis of a rectangular domain with a particular spacing based on Ramachandran *et al.* work [41] (see Fig.3.4.b). A global Nusselt number can be computed based on each sphere contribution (see Fig.3.4.c).

Euzenat [38] found that for coarse meshes, heat transfer may be underestimated. It can reach a plateau and then converges for high refinements, hence the importance to undertake a grid convergence study on the interfacial heat flux.

He also found through its three particles configuration that the rate of convergence was different for each bubble. The two first spheres are equally spaced while the third one is closer to the domain outlet. Consequently, for high Pe , the first sphere experiences higher velocity (and also drag force and heat transfer) while the others, in the wake of the first sphere, are facing less important velocity and temperature gradient.

Consequently, depending on the particle distribution, Euzenat observes that the rate of convergence is not the same over the particles. Assessing the algorithm and its convergence based on a general Nusselt may be risky. It is thus advisable to perform several local Nusselt convergence studies even for a random array of multiple spheres.

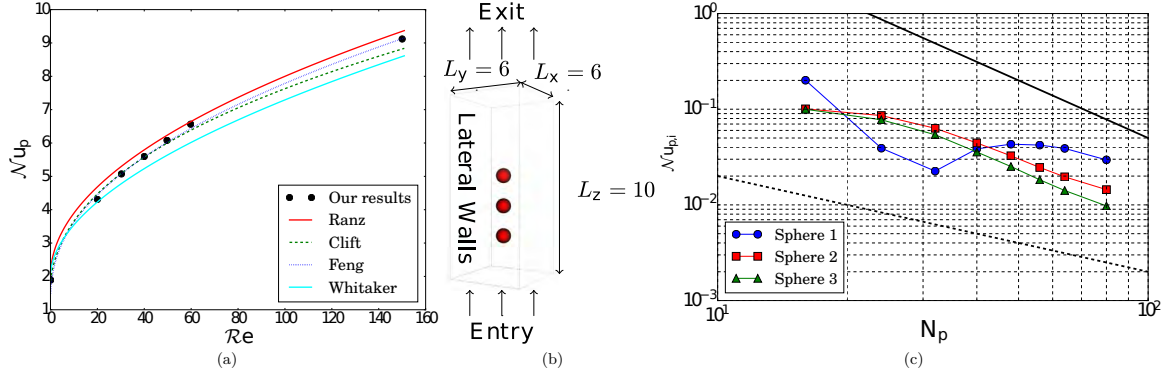


Figure 3.4: (a) Comparison of the Nusselt number between literature correlations and Euzenat's results [38]
 (b) More complex configuration: three in-line particles
 (c) Local Nusselt numbers on each sphere

Finally, in the line of their diffusion-growth combination (phase change), Tanguy *et al.* [9] have tested their implementation using a supplementary test involving convection: the rise of a growing bubble. Gravity effect was enabled to ensure movement.

As previously, bubble temperature is set as the saturation temperature. In a particular range of Peclet number (Pe), an expression relating the Nusselt number to the Peclet number has been already investigated [42] (see Eq.3.15).

$$Nu = \frac{4}{\sqrt{3\pi}} \sqrt{Pe} \quad (3.15)$$

In conclusion, it is important to notice that the correlations are only valid at constant bubble/particle temperature (or non-dimensionalised concentration [24]) or assuming a homogeneous distribution due to a high sphere conductivity. In the case of phase change, the temperature is imposed at the saturation temperature inside the bubble. In our case, both bubble and domain temperatures are varying as the implemented boundary conditions are not allowing to constrain the bubble temperature. A steady-state simulation is then not possible. It will be shown later (sections 4.2.2 and 5.1.2) that we can hope to obtain a quasi-asymptotical value of the Nusselt number on a narrow range of time by choosing certain physical parameters in the vapour phase. It is important to remember that the values of the Nusselt number from the various correlations are theoretically the highest reachable values.

The more interesting way to check the heat transfer in our program at low cost is undoubtedly using the same methodology as Legendre [24] but using correlations for viscous bubbles at high Reynolds numbers and for several viscosity ratios [16] (see Eq.3.14). A flow-field velocity can be imposed in the form of a bubble terminal velocity. Fluid viscosities and Prandtl numbers are then chosen according to the design of experiments of swarms and channels. The results of this validation are presented in section 5.1.

Chapter 4

Methodology

4.1 TrioIJK: from governing equations to numerical methods insight

TrioIJK uses a method referred to as the one-fluid formulation where a single set of equations is used to describe the two fluids. Parameters such as viscosity, conductivity, heat capacity or density are calculated based on each cell fluid fraction and updated over time. The local or continuous formulation is easy to develop but its discretisation over a cell when the problem is translated to a finite volume formulation is difficult to handle.

This one fluid formulation will be presented in both momentum, mass and energy equation. Its discretisation will be later dealt with in depth, in sight of results and observations on the energy conservation and local errors in the temperature field (section 5.1).

A quick explanation about phase-averaging the energy equation to perform a closure on a two-fluid model (Euler-Euler) is described in Appendix C. As a reminder, the averaged DNS post-processed values will potentially be used later by Aymeric Sonolet in a machine-learning algorithm to deduce models for the different unknowns of the averaged equation (e.g. the interphase unknown, turbulent heat flux...).

Finally, the methodology for both validation in pure diffusion and convection will be detailed.

4.1.1 One-fluid formulation of the Navier-Stokes equations

The simulated multi-phase flows are incompressible. The local resolution implies to solve the Navier-Stokes equations directly at the cost of several requirements and considerations such as constant physical properties over each Newtonian fluid phase and a massless interface.

Each phase is verifying the Navier-Stokes equations over its domain. By denoting $k = [v, l]$ the subscript of each phase where v stands for vapour and l for liquid, the mass continuity and the momentum equation can be formulated as follows:

$$\begin{cases} \frac{\partial \rho_k}{\partial t} + \nabla \cdot (\rho_k \mathbf{v}_k) = 0 \\ \frac{\partial \rho_k \mathbf{v}_k}{\partial t} + \nabla \cdot (\rho_k \mathbf{v}_k \mathbf{v}_k) - \rho_k \mathbf{g} - \nabla \cdot (-P_k \mathbf{I} + \boldsymbol{\tau}_k) = 0 \end{cases} \quad (4.1)$$

where ρ_k , p_k and \mathbf{v}_k refer to the density, the pressure and the velocity in phase k . \mathbf{g} denotes the gravitational acceleration while the stress tensor is denoted by $\boldsymbol{\tau}_k = \mu_k (\nabla \mathbf{v}_k + \nabla^T \mathbf{v}_k)$

To these two equations, some relation should be defined to solve the properties' jump at the interface. For an adiabatic and isothermal flow, two conditions arise. The velocity at the interface is continuous in both tangential \mathbf{t} and normal directions \mathbf{n} while the pressure and stress jump is compensated by the forces coming from the surface tension as it is summarised in the following system of equation [4]:

$$\begin{cases} v_v^n = v_l^n \text{ & } v_v^t = v_l^t \\ \sum_{k \in [v,l]} (p_k \mathbf{n}_k - \tau_k \cdot \mathbf{n}_k) = \sigma \kappa \mathbf{n} \end{cases} \quad (4.2)$$

where σ is the surface tension. The local curvature can be expressed depending on the local normal unit vector at the interface such as $\kappa = \nabla_s \cdot \mathbf{n}$. By neglecting the fluctuations of the surface tension $\nabla \sigma = 0$ i.e. the Marangoni effect, the interface conditions have been simplified.

Navier-Stokes equations in both phases can thus be combined by using the indicator function χ_k i.e. the Heaviside 3D function. In other words, the indicator function linked to a phase k is theoretically equal to 1 in the phase k and 0 otherwise. It will be seen later that once integrated over a control volume split by the interface, the discretised indicator function denoted $I_k = \int_V \chi_k dV / \int_V dV$, can be in the whole range $[0, 1]$. The normal unit vector can also link the phase indicator gradient to the Dirac impulsion such as $\nabla \chi_v = -\mathbf{n} \delta^i$.

Any one-fluid flow parameter ϕ can be deduced from each phase using the indicator function and its associated rules:

$$\phi = \sum_{k=[v,l]} \chi_k \phi_k \text{ with } \chi_k^n = \chi_k, \chi_v \chi_l = 0 \quad (4.3)$$

The goal is to solve directly for ϕ using only one formulation of the Navier-Stokes equations. Interface is solved implicitly according to simplifications and it only needs to solve a supplementary equation to transport the indicator χ_k (I_k once integrated over a cell).

First the mass continuity equation can be multiplied by the indicator function χ_k . Using the derivative rule of product, it leads to the final equation 4.4 for the mass continuity.

$$\frac{\partial \rho_k \chi_k}{\partial t} + \nabla \cdot (\chi_k \rho_k \mathbf{v}_k) - \rho_k \left(\frac{\partial \chi_k}{\partial t} + \mathbf{v}_k \cdot \nabla \chi_k \right) = 0 \quad (4.4)$$

Where $\partial \chi_k / \partial t + \mathbf{v}_k \cdot \nabla \chi_k = 0$ is the advection equation for the indicator function χ_k i.e. the transport equation of the interface by the local velocity. It finally gives equation 4.5.

$$\frac{\partial \rho_k \chi_k}{\partial t} + \nabla \cdot (\chi_k \rho_k \mathbf{v}_k) = 0 \quad (4.5)$$

Using the same method for the momentum equation leads to equation 4.6.

$$\frac{\partial \rho_k \chi_k \mathbf{v}_k}{\partial t} + \nabla \cdot (\chi_k \rho_k \mathbf{v}_k \mathbf{v}_k) = -\nabla \cdot (\chi_k P_k \mathbf{I} - \chi_k \tau_k) + \chi_k \rho_k \mathbf{g} + (P_k \mathbf{I} - \tau_k) \nabla \chi_k \quad (4.6)$$

By adding up both mass continuity and momentum equations on each phase, the one-fluid flow formulation of the Navier-Stokes equations is obtained (system of equations 4.7).

$$\begin{cases} \frac{\partial \rho}{\partial t} + \nabla \cdot (\rho \mathbf{v}) = 0 \\ \frac{\partial \rho \mathbf{v}}{\partial t} + \nabla \cdot (\rho \mathbf{v} \mathbf{v}) = -\nabla \cdot (P \mathbf{I} - \tau) + \rho \mathbf{g} + \sigma \kappa \mathbf{n} \delta^i \end{cases} \quad (4.7)$$

The aim of formulating this one-fluid equation is to solve only one set of the Navier-Stokes equation over the entire domain while solving for the interfacial terms and including the jump conditions.

4.1.2 One-fluid approach for the temperature equation

A previous PhD student implemented and studied the dynamics of bubble swarms using the one-fluid formulation [4]. Current research is now focused on thermal effects. That is why a similar approach has been undertaken by the laboratory.

The essence is the same but written in term of the temperature (scalar T_k) in each phase with their associated thermal physical parameters Cp (heat capacity) and λ_k (thermal conductivity). α is often used to denote the thermal diffusivity but here, D is used instead. α_k is used here to represent the statistic average of the indicator function χ_k such as $\alpha_k = \bar{\chi}_k$. The temperature equation expressed in phase k is represented by:

$$\frac{\partial(\rho_k C p_k T_k)}{\partial t} + \nabla \cdot (\rho_k C p_k T_k \mathbf{v}_k) = \nabla \cdot (\lambda_k \nabla T_k) \quad (4.8)$$

Once multiplied by the indicator function χ_k , the equation can be re-ordered to obtain:

$$\begin{aligned} & \left[\frac{\partial(\chi_k \rho_k C p_k T_k)}{\partial t} + \nabla \cdot (\chi_k \rho_k C p_k T_k \mathbf{v}_k) \right] - \rho_k C p_k T_k \left[\frac{\partial \chi_k}{\partial t} + \mathbf{v}_k \nabla \cdot \chi_k \right] \\ &= \nabla \cdot (\chi_k \lambda_k \nabla T_k) - \lambda_k \nabla T_k \cdot \nabla \chi_k \end{aligned} \quad (4.9)$$

Finally, the transport equation of χ_k , equal to zero, appears and the final solution over the phase k is established as shown in the following equation:

$$\frac{\partial(\chi_k \rho_k C p_k T_k)}{\partial t} + \nabla \cdot (\chi_k \rho_k C p_k T_k \mathbf{v}_k) = \nabla \cdot (\chi_k \lambda_k \nabla T_k) - \lambda_k \nabla T_k \cdot \nabla \chi_k \quad (4.10)$$

By adding up the two equations, written for each phase, and as $\nabla \chi_k = -\mathbf{n} \delta^i$ where δ^i stands for the dirac delta function at the interface, we can write the equation without the indicator function χ_k (Eq.4.11).

$$\frac{\partial(\rho C p T)}{\partial t} + \nabla \cdot (\rho C p T \mathbf{v}) = \nabla \cdot (\lambda \nabla T) + \left[\sum_{k \in [v, l]} \lambda_k \nabla T_k \cdot \mathbf{n} \delta_k^i \right] \quad (4.11)$$

Without phase-change, the continuity of the flux at the interface in the normal direction expressed by the relation 4.12, allows us to reduce the equation 4.11 to equation 4.13.

$$\lambda_0 \frac{\partial T}{\partial n} \Big|_0 = \lambda_1 \frac{\partial T}{\partial n} \Big|_1 \Leftrightarrow \sum_{k \in [v, l]} \lambda_k \nabla T_k \cdot \mathbf{n} \delta_k^i \quad (4.12)$$

$$\frac{\partial(\rho C p T)}{\partial t} + \nabla \cdot (\rho C p T \mathbf{v}) = \nabla \cdot (\lambda \nabla T) \quad (4.13)$$

We can notice that it corresponds to the conservative form of the equation ($\rho C p T$ inside the temporal and divergence terms). To obtain a finite volume formulation of this equation, it needs to be integrated and averaged over a control volume V_c before applying the divergence theorem (see Eq.4.14). It will be shown later that in the case of split cells, several choices are available to calculate the one-fluid parameters ρ , Cp and λ properly.

$$\frac{\partial}{\partial t} \left[\frac{1}{V_c} \int_{V_c} \rho C p T dV \right] + \frac{1}{V_c} \int_{S_c} \rho C p T \mathbf{v} \cdot \mathbf{n}_S dS = \frac{1}{V_c} \int_{S_c} \lambda \nabla T \cdot \mathbf{n}_S dS \quad (4.14)$$

Alternatively, the non-conservative form can be written from eq.4.13 as:

$$\frac{\partial}{\partial t} \left[\frac{1}{V_c} \int_{V_c} T dV \right] + \frac{1}{V_c} \int_{S_c} T \mathbf{v} \cdot \mathbf{n}_S dS = \frac{1}{V_c} \int_{S_c} \frac{1}{\rho Cp} \lambda \nabla T \cdot \mathbf{n}_S dS \text{ where } \frac{1}{\rho Cp} = \sum_k \frac{\chi_k}{\rho_k C_p k} \quad (4.15)$$

4.1.3 Discretisation of the one-fluid terms

As the discretisation of the equation will be clarified later, a brief explanation concerning the discretisation of the one-fluid parameters is given in this section. For example, the one-fluid cell temperature \hat{T} is calculated by integrating the continuous indicator function over the cell and by defining the average phase temperature $\langle T \rangle_k^c$:

$$\hat{T} = \frac{1}{V_c} \int_{V_c} \sum_{k \in [v,l]} T_k \chi_k dV = \sum_{k \in [v,l]} \frac{1}{V_c} \int_{V_c} T_k \chi_k dV = \sum_{k \in [v,l]} \langle T \rangle_k^c I_k^c \text{ with } I_k^c = \frac{\int_{V_c} \chi_k dV}{V_c} \quad (4.16)$$

4.2 Temperature equation implementation and validation

4.2.1 Validation of the diffusion on a fixed spherical bubble in a quasi-infinite domain and quiescent liquid

To validate the first part of the thermal algorithm implementation *i.e.* without any convection or phase change, a bubble (fluid or solid) of diameter $d = 2\text{mm} = 2R$ is initialised at the centre of a cubic domain (fluid) of width $a = nd$ (n large enough to consider an infinite domain).

A temperature difference between the two phases is set using the discretised indicator function denoted by the variable I_l (1 outside the bubble, 0 inside the bubble, $0 < I_l < 1$ for the elements shared by the two sub-domain at the interface). The resulting temperature field will be studied along the radial axis (spherical coordinates) over time.

The solution computed by TrioIJK will be compared to the results obtained from 1D finite volume-difference simulations in the style of Das *et al.* [5]. However, the discretisation of the cell and face centres in the uni-axial direction is offset (Fig.4.1).

Compared to Das *et al.*, at the cell n_1 , we do not need $n_1 + 1$ to compute the flux balance but only the interface temperature $*$, still in the same domain. Das used a ghost fluid approach which requires a more complex formulation as the properties are changing on a cell face and not on a cell node like in our case.

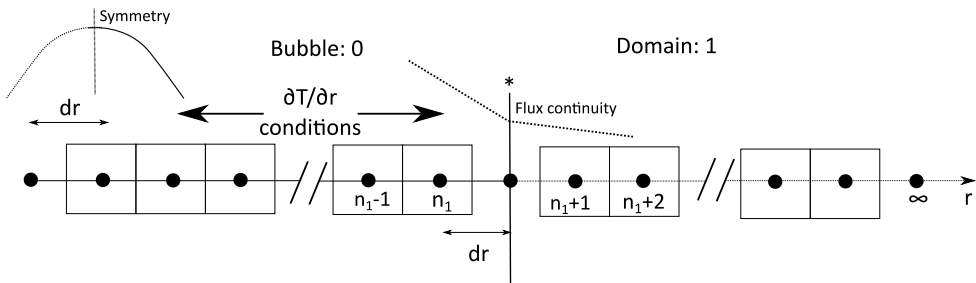


Figure 4.1: Modified 1D finite-difference formulation of the problem being inspired by Das *et al.* [5]

The implementation of this simplified algorithm is assessed using Panda *et al.* data [6]. The system of equations for diffusion is solved in spherical coordinates along the radial axis and is given by the

following system of equation (Eq. 4.17):

$$\left\{ \begin{array}{l} \frac{\partial T}{\partial t} = \frac{D_0}{r^2} \frac{\partial}{\partial r} \left(r^2 \frac{\partial T}{\partial r} \right) \quad r \leq R \\ \frac{\partial T}{\partial t} = \frac{D_1}{r^2} \frac{\partial}{\partial r} \left(r^2 \frac{\partial T}{\partial r} \right) \quad R \leq r \leq R_\infty \end{array} \right. \quad \text{and} \quad \left\{ \begin{array}{l} r = 0 \quad \frac{\partial T}{\partial r} = 0 \\ r = R_\infty \quad T = T_1 \\ r = R \quad T_0 = T_1, -\lambda_0 \frac{\partial T}{\partial r} \Big|_0 = -\lambda_1 \frac{\partial T}{\partial r} \Big|_1 \\ t = 0 \quad T = T_0, T = T_1 \end{array} \right. \quad (4.17)$$

Where D_0 and D_1 are the diffusion coefficient of the bubble and the fluid domain respectively such as $D_i = \lambda_i / (\rho_i C p_i)$.

To this 1D equation, we add spatial boundary conditions (BC) to take into account the symmetry, a constant infinite temperature field and finally the temperature and heat flux continuity at the interface. Initial conditions are also required. They are summarised in equation 4.17. Temperature is discretised using a backward 2^{nd} order finite difference scheme for the temporal term (1^{st} order for the first iteration) while the spatial term is discretised using a central difference scheme at the 2^{nd} order and finally a forward 2^{nd} order for the zero derivative condition at $r=0$. The combination is stable.

If the time discretisation is quite obvious, the spatial discretisation may be done differently by approaching the problem using a non conservative finite difference versus a finite volume method. In the finite volume method, the conservation of quantities in a control volume is ensured. Then, the operator $\nabla \cdot (\lambda \nabla T)$ can be approximated considering a balance between the two cell-faces at $i + 1/2$ and $i - 1/2$:

$$\frac{\partial}{\partial r} \left(r^2 \frac{\partial T}{\partial r} \right) \Big|_i = \frac{r_{i+1/2}^2 \frac{\partial T}{\partial r} \Big|_{i+1/2} - r_{i-1/2}^2 \frac{\partial T}{\partial r} \Big|_{i-1/2}}{\Delta r} = \frac{r_{i+1/2}^2 (T_{i+1} - T_i) - r_{i-1/2}^2 (T_i - T_{i-1})}{\Delta r^2} \quad (4.18)$$

It is also sometimes referred to conservative finite difference formulation. Discretised equation can be finally expressed as follows (Eq.4.19) where i stands for the spatial subscript while j is the time superscript.

$$\frac{1}{2\Delta T} [3T_i^{j+1} - 4T_i^j + T_i^{j-1}] = \frac{D_i}{r_i^2 \Delta r^2} [r_{i-1/2}^2 T_{i-1}^{j+1} - (r_{i-1/2}^2 + r_{i+1/2}^2) T_i^{j+1} + r_{i+1/2}^2 T_{i+1}^{j+1}] \quad (4.19)$$

The system can be re-written into a linear system to solve at time iteration $j + 1$ (see Eq. 4.20).

$$A^j T^{j+1} = B^{j-1,j} \leftrightarrow T^{j+1} = (A^j)^{-1} B^{j-1,j} \quad (4.20)$$

By combining the continuity of the heat flux and the temperature at the interface, Das *et al.* [5] established an equation of the temperature at the interface denoted T^* . The finite difference coefficients were found in Das' paper assuming the interface was at a distance $dr/2$ and $3dr/2$ from points $(n_1, n_1 + 1)$ and $(n_1 - 1, n_1 + 2)$, respectively. In our case, the interface is represented by a node *i.e.* separated by dr and $2dr$. It leads to a slightly different inter-facial temperature condition:

$$T^* = \frac{\lambda_0(4T_{n_1} - T_{n_1-1}) + \lambda_1(4T_{n_1+1} - T_{n_1+2})}{3(\lambda_0 + \lambda_1)} \quad (2^{nd} \text{ order}) \quad (4.21)$$

Temperature and fluid/solid parameters used for both 1D and 3D simulations are based on Panda *et al.* study [6]. They checked the implementation of their diffusion algorithm using three different combinations: vapour/fluid, solid/vapour and solid/gas (see table 4.1).

Table 4.1: Phase and domain properties

Physical properties	Units	Air	Water	Alumina (solid)
Density ρ	$\text{kg} \cdot \text{m}^{-3}$	1.2	1000	4000
Heat Capacity C_p	$\text{J} \cdot \text{kg}^{-1} \cdot \text{K}^{-1}$	1.0×10^3	4.2×10^3	9.0×10^2
Thermal conductivity k	$\text{W} \cdot \text{m}^{-1} \cdot \text{K}^{-1}$	3.0×10^{-2}	6.0×10^{-1}	3.0×10^1
Thermal diffusivity D	$\text{m}^2 \cdot \text{s}^{-1}$	2.5×10^{-5}	1.4×10^{-7}	8.3×10^{-6}
Domain properties		Air-Water	Alumina-Air	Alumina-Water
Dimensions (m)	$L_x = L_y = L_z$	$5d = 0.01$	$15d = 0.03$	$6d = 0.12$
Elements (nb)	$N_x = N_y = N_z$	240	480	240

The temperature is initialised at $T_0 = 373$ K and $T_1 = 273$ K in both 1D and 3D simulations. The time step for the 1D case is chosen to be $dt_{1D} = 2 \times 10^{-4}$ s and is coupled with a grid resolution $d/\Delta r = 80$ which has led to convergence according to Panda *et al.*.

The 3D domain is set to match the 1D configuration and the condition on the domain size (see table 4.1). L_i , N_i stand respectively for the length, number of cells. The subscripts x , y and z indicate the different directions. The thermal time step is generated using the Fourier number Fo i.e. the ratio of the diffusion and storage energy (Eq.4.22). It can be shown that it is a condition of stability ensured by an amplification factor lower than unity. Lower values of Fo would not improve the results but would slow down the simulations.

$$Fo = \frac{Dt}{L^2} \rightarrow t = \frac{FoL^2}{D} \Rightarrow \Delta t = \frac{1}{6} \frac{d_{(x,y,z)_{min}}^2}{\alpha_{min}} \quad (4.22)$$

Periodic boundary conditions are used on each axis x , y and z . Gravity is disabled and a zero velocity field is initialised. Finally, the results are reported using a normalised temperature field $\Phi = (T - T_1)/(T_0 - T_1)$ i.e. $T = T_0$ leads to $\Phi = 1$ and for $T = T_1$, $\Phi = 0$. A normalised radius $\tilde{r} = r/R$ is also defined to get $\tilde{r} = 1$ at the interface.

4.2.2 Convection validation: rise of a spherical bubble

Protocol and dimensionless parameters selection

To validate the convection implementation, a similar approach to the one of Figueroa and Legendre [24] has been chosen. However, instead of using an inviscid bubble, our simulation will involve a viscous one. A fixed spherical bubble in a moving fluid is then mimicking a rising bubble in a quiescent fluid domain (see figure 4.2.a). We are highly limited by the boundary conditions which are only available in the code for swarm and channel simulations. In addition, some well-known momentum conservation issues arise with the numerical method and they can lead to slight temporal deviation. Consequently, it is not obvious to obtain the desired (almost) steady-state and flow conditions (dynamics and thermal).

First, the code is not supporting a variable grid spacing. As a consequence, the spatial resolution in the far-field is theoretically too fine. Consequently, the chosen domain is relatively narrow to keep a reasonable computational power. The solution may differ from the solution of an infinite domain. The boundary layer will be compressed leading the bubble to slow down compared to an infinite domain. It has been more and more noticeable with an increasing Reynolds number and an increasing viscosity ratio. However, the selected domain ($2.5dx2.5dx10d$) is large enough to get reasonable results.

The convection validation should be realised over a sufficiently large Reynolds number range. A major part of the swarm simulations are planned to be realised at a Reynolds number value of 400. In this case, particular attention has been given to the effect of spatial discretisation. Then, several

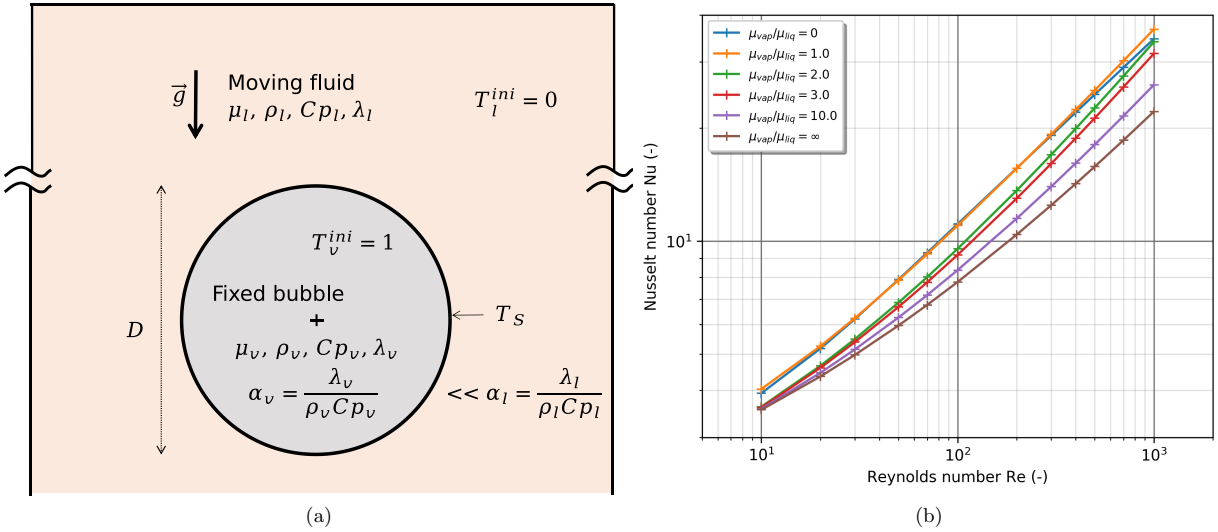


Figure 4.2: (a) Schematic of the simulated configuration: a viscous and spherical fixed bubble mimicking a rising bubble, (b) Nusselt number correlation for a liquid Prandtl number $Pr = 1$ [37]

simulations were initialised in the theoretical range of $Re = [10; 800]$. The desired Reynolds number can not be achieved by simply initialised an inlet velocity. In swarms simulations, the gravity is obviously taken into account. Therefore, the liquid viscosity μ_l is tuned to reach a terminal velocity so the desired Reynolds number while keeping the desired viscosity ratio.

If re-write the Reynolds number, we can see that it depends on the terminal velocity (see Eq.4.23) and therefore on the Drag coefficient C_d .

$$Re = \frac{\rho_l V_{term} D}{\mu_l} = \frac{\rho_l D}{\mu_l} \sqrt{\frac{2(\rho_l - \rho_v) g V}{\rho_l A_p C_d}} = \frac{K}{\mu_l \sqrt{C_d}} \text{ with } K = \text{const and } A_p \text{ the projected area} \quad (4.23)$$

Using an appropriate correlation, as the one proposed by Feng and Michaelides [16, 43], can help us find out the theoretical terminal velocity for a given Reynolds number and viscosity ratio. Then, an approximate value of liquid viscosity can be found. It helps to get closer to the desired flow configuration. However, the Reynolds number observed turns out to be lower than expected due to previous domain size effects and the accuracy of the correlation.

From targeted values $Re = 10$ to $Re = 400$, the prediction looks better for the tested viscosity ratio 0.1 for whom it is was noticeable that the flow was stabilising faster. Above this Reynolds number value, the simulations involving the viscosity ratio $\mu_v/\mu_l = 1$ were evolving very slowly. The ones at $\mu_v/\mu_l = 0.1$ were stabilised but the effect of the domain was more and more visible as the Reynold number measured turns out to be 580 instead of the theoretical Reynolds of 800. Based on these observations the dynamics of simulations involving a theoretical Reynolds number of 600 and 800 at $\mu_v/\mu_l = 1$ should be greatly mispredicted. However, because of the slow behaviour of these two simulations, we have decided to stop them but still considered them in our study. As they are not fully stabilised, their Reynolds number is not as far from the theoretical value compared in the other (fully stabilised) simulations.

Finally, Feng *et al.* [37] underlines in many of their papers that the density ratio is not particularly modifying the dynamics of a spherical bubble. As underlined multiple times, the aim of the simulations is also to be compared to experimental data involving Freon R12. As a consequence, the densities will be chosen as the vapour and liquid density of Freon R12 at around 15 bars. Two ratios of viscosities are tested as highlighted previously: 1 and 0.1 (Freon R12) which are enough for our needs.

The dynamics of the flow is then governed by the following dimensionless variables: the bubble Reynolds number Re , the viscosity ratio μ_v/μ_l , the density ratio ρ_v/ρ_l and the Eotvos number equal to 0.1 to keep globally a spherical shape while limiting the surface tension effect on the time-step limitations.

Finally, the bubble is fixed using an isotropic spring and damping term in the Navier-Stokes equations. It has been observed through previous laboratory work that the spring force applied to the bubble is acting to compensate the numerical error ε (The previous spring and damper coefficients of $3e5$ and $-1.5e-3$ have been used). It has been seen that the bubble is stabilising in an oscillatory regime at high Reynolds numbers.

At high Reynolds numbers, it is true that a rising viscous bubble is no longer showing a linear trajectory but rather a zig-zag path or a helicoidal one as it transitions into a turbulent state via an unsteady wake. However, the spring force may play a role in the observed transverse oscillations amplitude. We can ask ourselves if the spring force in these transverse directions is acting too much against any small disturbances. In other words, these oscillations might be overshoots brought by the spring force. By lack of time, the eventual coupling between the physical effect and the force induced oscillations has been neglected as they will not drastically impact the heat transfer. The dynamics and the bulk velocity is considered sufficiently stabilised to run the thermal part of the algorithm.

Now that the dynamics are initialised, the heat capacity Cp_v and the conductivity λ_v in the vapour phase needs to be chosen to mimic as much as possible a constant bubble temperature or concentration situation. In other words, a constant bubble temperature constitutes the theoretical maximum heat transfer situation for given dynamics.

We wanted at first to choose a reasonably high ρ_vCp_v to retain the vapour phase decrease in temperature for long enough to obtain a stabilised Nusselt number. It will be shown in section 5.1 that some energy is lost from the vapour phase due to numerical issues mostly (in addition to physical heat transfers). For a given Prandtl number Pr_v , when $\rho C p_v$ increases, it first affects the temperature distribution in the liquid and the interfacial flux. Then, above a certain value (threshold), the impact of further increasing $\rho C p_v$ becomes negligibly small because of the vapour spurious energy loss. The ρ_vCp_v value has been fixed by the ratio $\rho_vCp_v/\rho_lCp_l = 10$.

The Prandtl number reveals how the diffusion process is small compared to the convection one, hence leading to more homogeneous temperature fields when the Prandtl number decreases. Various vapour Prandtl number have also been tested to keep the bubble temperature variation within 10% of its mean value. A Prandtl number of 0.05 has been chosen and set through the vapour conductivity λ_v . Lowering the Prandtl would have homogenised more the bubble temperature at the cost of further decreasing the time-step.

The liquid properties are chosen according to the Prandtl number $Pr_l = \mu_l C p_l / \lambda_l$. As for the viscosity ratio, two Prandtl numbers of 1 and 2.62 for Freon R12 are investigated. The Freon conductivity $\lambda_l = 0.055 \text{ W.K}^{-1}.\text{m}^{-1}$ is used to describe the liquid phase. The physical parameters are summarised in table 4.2.

Nusselt number processing and energy reconstruction errors

To compute the Nusselt number, several methods are possible. An inlet-outlet energy balance could be used but it is not the most suited solution because of the periodicity of the domain. Then it could be possible to compute the heat flux leaving the bubble. However, it implies to find the temperature gradient near the bubble which is not handy due to the discontinuities of both the conductivity and the temperature gradient. As we are computing the one-fluid temperature inside the split cells, it requires

Table 4.2: Summary of parameters tested. The velocity V_{term} in the definition of Re_b is estimated based on the correlation. The actual Re_b obtained in the simulation will be slightly different

Effect	Dimensionless parameter	Expression	Tested Values
Dynamics	ρ_v/ρ_l	-	0.075
	μ_v/μ_l	-	0.1 – 1
	$Eo(\rho_l, \rho_v, \sigma)$	$(\rho_l - \rho_v) D^2 g / \sigma$	0.1
	$Re_b(\mu_l, \rho_l)$	$\rho_l V_{term} D / \mu_l$	10 – 50 – 100 – 200 – 400 – 600 – 800
Heat transfer	$Pr_l(\mu_l, Cp_l, \lambda_l)$	$\nu_l/D_l = \mu_l C p_l / \lambda_l$	1 – 2.62
	$\rho_v C p_v / \rho_l C p_l$	-	$10 \underbrace{(1000 - 10^5)}_{\text{Attempts}}$
	$Pr_v(\mu_v, Cp_v, \lambda_v)$	$\nu_v/D_v = \mu_v C p_v / \lambda_v$	0.05 $\underbrace{(0.1 - 0.5 - 1 - 10)}_{\text{Attempts}}$
Swarm effect	α	V_v/V_{tot}	0.8%

a supplementary algorithm to retrieve the exact phase temperature from whom the gradient could be computed.

The solution is to track the total thermal energy of the phase k through its average temperature $\langle T \rangle_k$. The heat transfer can be computed from the rate of stored energy scaled by the phase volume V_k as in equation 4.24.

$$Q_k(t_i) = \rho_k C p_k V_k \frac{\langle T \rangle_k(t_{i+1}) - \langle T \rangle_k(t_{i-1})}{t_{i+1} - t_{i-1}} \quad (4.24)$$

Then the Nusselt number can be computed from the heat Q_k , the vapour-liquid temperature difference ($\langle T \rangle_v(t_i) - \langle T \rangle_l(t_i)$) and the bubble surface area A .

$$Nu_k(t_i) = \frac{h_k(t_i)D}{\lambda_l} = \frac{Q_k(t_i)D}{\lambda_l A (\langle T \rangle_v(t_i) - \langle T \rangle_l(t_i))} \quad (4.25)$$

The Nusselt number is commonly defined according to the surface temperature T_S and an infinite field temperature T_∞ . However, in swarms studies, the domain is tri-periodic which leads the cold temperature T_∞ to change over time. Moreover, the heat transfer is defined between the two phases. Instead of evaluating a local Nusselt number for each bubble, it is more interesting to define a global Nusselt number according to the average phase temperature difference. In the case where a single bubble tends to be at constant temperature, ($\langle T \rangle_v - \langle T \rangle_l \rightarrow (T_S - T_\infty)$).

$\langle T \rangle_k$ can be deduced from average phase temperature values $\langle T \rangle_k^c$ in each cell c . By definition:

$$\langle T \rangle_k = \frac{\int_V T \chi_k dV}{\int_V \chi_k dV} = \frac{\sum_c \frac{1}{V_c} \int_{V_c} T \chi_k dV}{\sum_c \frac{1}{V_c} \int_{V_c} \chi_k dV} = \frac{\sum_c \langle T \rangle_k^c I_k^c}{\sum_c I_k^c} \quad (4.26)$$

However, in the mixed cell, the temperature $\langle T \rangle_k^c$ is not directly accessible. We are doing an approximation by assuming that the average phase temperature equals the average cell temperature \hat{T} such as $\langle T \rangle_k^c \approx \hat{T}$. In other words, $\langle T \rangle_k \approx \sum_c \hat{T} I_k^c / \sum_c I_k^c$. This approximation is theoretically valid only in the absence of a temperature gradient normal to the interface. Slight discrepancy might arise only in the interface vicinity, when strong normal heat flux occurs.

Alternatively, the heat can be computed from the energy variation $Q_k = dE_k/dt$. Energy has been post-processed using the same approximation on the average phase temperature. In a cell, the energy

E_k^c can be expressed as:

$$\frac{E_k^c}{V_c} = \rho_k C p_k \frac{1}{V_c} \int_{V_c} T \chi_k dV \leftrightarrow E_k^c = \rho_k C p_k V_c \langle T \rangle_k^c I_k^c \quad (4.27)$$

If we look at the vapour phase energy in a mixed cell we can express the reconstruction error as follows:

$$\frac{E_v^c}{V_c} = \rho_v C p_v I_v^c \langle T \rangle_v^c = \rho_v C p_v \left[(I_v^c + I_l^c) \hat{T} - I_l^c \langle T \rangle_l^c \right] = \underbrace{\rho_v C p_v I_v^c \hat{T}}_{\text{Post-Processed}} + \underbrace{\rho_v C p_v I_l^c (\hat{T} - \langle T \rangle_l^c)}_{\text{Reconstruction error}} \quad (4.28)$$

When the spatial resolution is enhanced, the average temperature $\langle T \rangle_v$ and $\langle T \rangle_l$ in mixed cells should get closer due to the continuity of temperature at the interface, hence leading to the assumption $\hat{T} = \langle T \rangle_v = \langle T \rangle_l$ to be more and more acceptable.

Once computed, averaged Nusselt numbers can be compared to Feng *et al.* correlations [37] shown in figure 4.2.b. It is noticeable that the Michaelides predictions for low viscosity ratios ($\mu_{vap}/\mu_{liq} < 2$) are not as accurate as for higher ratios' because the correlation leads to a non-monotonic behavior with the ratio of viscosities. Feng and Michaelides tried to maximise the match between their set of data. Their correlation, over a wide range of parameter, is then showing small errors. In reality, the Nusselt number is strictly decreasing when the viscosity ratio is increased in comparison with figure 4.2.b. It will be taken into account in our conclusions.

Chapter 5

Results and discussions

5.1 Thermal algorithm implementation and accuracy assessment

5.1.1 Diffusion validation: a fixed spherical bubble in a quasi-infinite domain

In the original implementation, results were not conclusive and a huge error was observed at the interface. It was not an error related to convergence but rather to the formulation of the one-field parameters λ and ρCp as the temperature behaves unexpectedly and shows a high discontinuity. From these observations, the effects of the λ jump (conductivity) and the ρCp jump on the solution were studied separately.

Average thermal conductivity in two-phase cells

According to Patankar [44], it is recommended to use a mean harmonic formula for the λ value in the cells split by the interface to conserve the heat flux continuity (see the demonstration in Appendix.D).

Using a harmonic mean formula instead of a simple arithmetic one also allows favouring the fluid with lower property value in the two-phase cells. In other words, a harmonic mean is virtually displacing the interface towards the lower viscosity region *i.e.* the bubble domain [1]. At $\rho Cp = const$, the effect of the mean formula can be observed in Fig.5.1.a and Fig.5.1.b. This validation and the subsequent reference results presented in this section refers to the setup described in section 4.2.1.

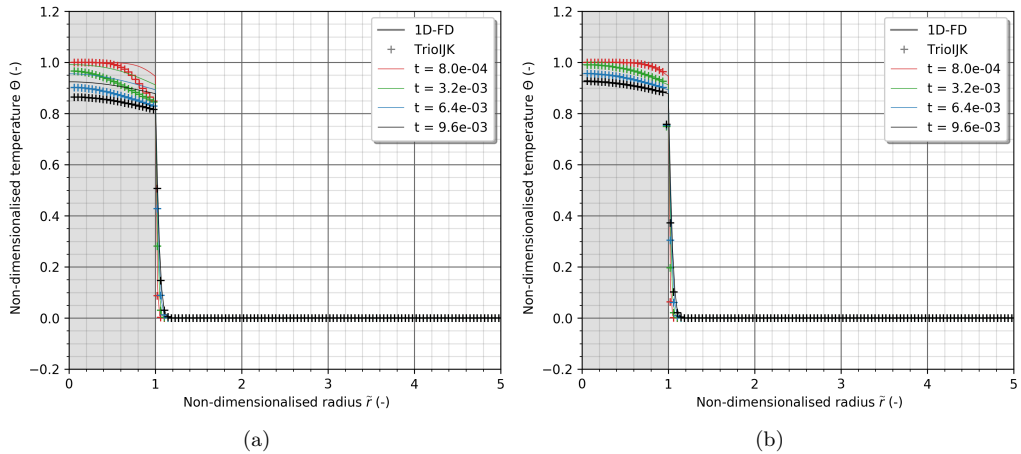


Figure 5.1: Effect of the mean λ calculation on the solution ($\alpha_{vap}/\alpha_{liq} \approx 200$). 1D-FD represents the reference solution.

$$(a) \text{ Arithmetic } \lambda_a = \sum_k \lambda_k I_k^c, \quad (b) \text{ Harmonic } \frac{1}{\lambda_h} = \sum_k \frac{I_k^c}{\lambda_k} \text{ with } I_k^c = \frac{\int_{V_c} \chi_k dV}{V_c}$$

In this case of diffusion, where the heat flux is considered in the radial direction only, we can clearly see that the arithmetic formula, used to calculate the average conductivity in the two-phase cell in our

first implementation, leads to overestimate the heat transfer between the bubble and the surrounding fluid.

To complete, it is worth mentioning that we are using an isotropic value of λ . As shown in Appendix.D, the arithmetic mean formula should be used in the tangential direction. The problem is the same for dynamics with the viscosity. However, no second-order implementation of this type has been published yet according to Tryggvason [1]. He also underlines that in practice, interfaces tend to be aligned with the flow direction in a shear flow, so the harmonic mean viscosity is more accurate. Similar justifications concerning the use of the harmonic mean formula for the conductivity have not been found in the literature.

To conclude on the one-fluid conductivity, using a harmonic mean is compulsory in this case. However, as the code will be used in situations where the heat transfer will not be purely radial, it will be necessary to keep in mind this approximation and eventually check its proportion to validate globally this assumption.

It is also interesting to notice that the demonstration in Appendix.D involves the local phase temperature values at the cell faces to calculate the heat flux through it. The average conductivity is then translating by itself the two-phase nature of a cell.

However, the temperature used to evaluate the fluxes at the interface is the one-fluid temperature. It is then not fully consistent with the demonstration but it is a sacrifice that needs to be done during discretisation.

Concerning the conductivity, what is done in the code to calculate the fluxes consists in calculating an average conductivity $\lambda_{i+1/2}$ and $\lambda_{i-1/2}$ on each cell face from the two neighbouring cell centres. It is then used as part of a central difference scheme. The calculation of the harmonic conductivity should be eventually done directly at the cell face but it requires to offset the calculation of the discretised indicator function. The effect has not been investigated deeply as the results were good enough at this point. Moreover, the interface is never perpendicular to the cell faces and the approximations made when going from the simplified 1D case to the 3D one are multiple and are probably stronger than this detail.

These assumptions are necessary to solve the system without introducing new unknowns or useless complexity; they are the essence of numerical discretisation. It is done at the cost of small errors that will decrease with the resolution.

ρCp calculation in two-phase cells

At $\lambda = \text{const}$, the evolution of temperature when a jump of ρCp is considered was showing an unexpected behaviour with the initial code formulation as shown in figure 5.2.a. The temperature at the interface increases but should be between the two cell values. As the solution is evolving, the error is spread all over the domain.

To understand the problem, we need to go back to the governing equation (Eq.4.14). As a reminder, when the equation is written with a continuous indicator function χ_k , each one fluid parameter can be split using the rules $\chi_k^n = \chi_k$ (e.g. $\rho_k C p_k T_k \chi_k = (\rho_k C p_k \chi_k) (T_k \chi_k)$ with Einstein's convention of summation over k). It is no more valid when the term is integrated.

Instinctively, the first approach has been to approximate the integral of the temporal term in order to isolate the one-fluid temperature \hat{T} :

$$\frac{1}{V_c} \int_{V_c} \rho Cp T dV \approx \left[\frac{1}{V_c} \int_{V_c} \rho Cp dV \right] \left[\frac{1}{V_c} \int_{V_c} T dV \right] = (\rho Cp)_a \hat{T} \quad (5.1)$$

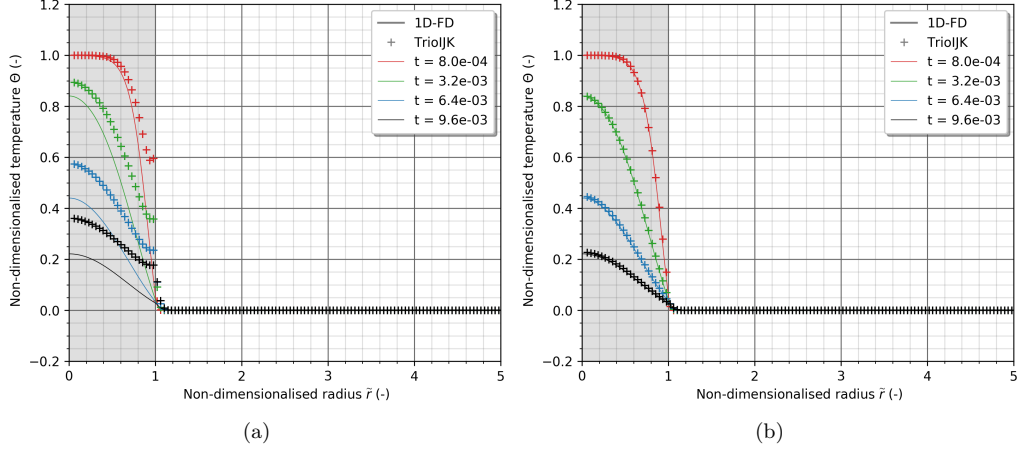


Figure 5.2: Effect of the ρC_p calculation on the solution ($\alpha_{vap}/\alpha_{liq} \approx 200$):

$$(a) \text{ Arithmetic } \frac{1}{(\rho C_p)_a} = \frac{1}{\sum \rho_k C p_k I_k^c}, \quad (b) \text{ Harmonic } \left(\frac{1}{\rho C_p} \right)_h = \sum_k \frac{I_k^c}{\rho_k C p_k} \text{ with } I_k^c = \frac{\int_{V_c} \chi_k dV}{V_c}$$

In this case, the one-fluid (ρC_p) parameter over a mixed cell correspond to the arithmetic mean of heat capacities: $(\rho C_p)_a = \sum_k \rho_k C p_k I_k^c$. According to the results, it is obvious that this approximation is false.

To be convinced, we can start from the true integral and decompose it onto the two phase volume $V_c = V_v + V_l$. Using the relation $I_v^c + I_l^c = 1$, we can make the arithmetic formula appear at the cost of a new terms (see full demonstration in appendix E.1.1):

$$\int_{V_c} \rho C p T dV = \underbrace{(\rho C p)_a \hat{T} V_c}_{\text{Solved}} + (\rho_v C p_v - \rho_l C p_l) I_l^c I_v^c V_c \underbrace{(\langle T \rangle_v^c - \langle T \rangle_l^c)}_{\text{Proportional to a flux } q} \quad (5.2)$$

This additional term is not cancelled. Using a simple 1D case, we can show that it is proportional to a certain interfacial flux q (see appendix E.1.2). In 3D, we can not provide a general formulation of this additional term, but the error will not be compensated.

Another trial has been to use a different initialisation such as $\hat{T}^{ini} = \sum_k \rho_k C p_k T_k^{ini} / (\rho C p)_a$ to start with a consistent energy in the mixed cells although the temperature solved was \hat{T} . The results were better, but thanks to the previous demonstration, we can conclude that it was probably because the additional terms were compensated enough by the initial excess of energy introduced in mixed cells. Even though this initial excess initially plays the role of the additional term, their time evolution will differ. The figures are available in section E.1.3 but not shown here to avoid a misunderstanding. Attentiveness is required to see the difference with the final results involving a harmonic formula. On this test case, the difference with the prediction by the harmonic formula is very small, but the theoretical justification of this approach does not seem to hold in more general cases and it has therefore been discarded.

The second approach was similar but using the non-conservative form of the equation. In this case, the harmonic mean formula for the ratio of ρC_p appears during the cell integration. The full demonstration based on the decomposition of the fluxes at the interface and cell sides is available in section E.2.

From equation 4.15 (without the convection term), we can develop the harmonic mean formula of the ratio of ρCp :

$$\int_{V_c} \nabla \cdot (\lambda \nabla T) dV = \left(\frac{1}{\rho Cp} \right)_h \int_{V_c} \nabla \cdot (\lambda \nabla T) dV + \left[\frac{1}{\rho Cp} \right] I_l^c I_v^c V_c \underbrace{\left[\int_{V_c} \nabla \cdot (\lambda \nabla T) dV - \int_{V_c} \nabla \cdot (\lambda \nabla T) dV \right]}_{=0} \quad (5.3)$$

seeing that the fluxes conservation at the interface leads to the equation $\int_{V_c} \chi_k \nabla \cdot (\lambda \nabla T) dV = V_c I_k^c \int_{V_c} \nabla \cdot (\lambda \nabla T) dV$ which seems a reasonable approximation. Basically, this approximation considers a weak variation in the cell of $\nabla \cdot (\lambda \nabla T)$ which is continuous (due to the conservation equation). This term is null when the temperature field is quasi-steady near the interface (by definition of a steady solution, the energy balance reduces to : $\nabla \cdot (\lambda \nabla T) = 0$). The results using the harmonic mean formula for $1/(\rho Cp)$ are shown in figure 5.2.b and comfort this assumption.

To conclude on the ρCp formulation, it is important to notice that both approaches make us split the integral to express the problem depending on the one-fluid temperature. Mathematically, the products of one-fluid parameters, once integrated, could not be split *a priori*. It has been proved that the heat flux assessment is valid when using a harmonic mean formula because of fluxes conservation in the control volume. In addition, the harmonic mean of ρCp is preferable as it only implies an assumption on the uniformity of $\nabla \cdot (\lambda \nabla T)$ which is less stringent than the assumption of uniform (one-fluid) temperature in mixed cells.

It might have been possible to look for solving directly for the energy ρCpT in a conservative form but it would imply an additional method to retrieve T used in the diffusive term and the crossed use of variables at different time steps (like ρ^n and $\rho^n + 1$).

Final results with corrections

Once the calculation of the one-fluid thermal parameters λ_h and $(1/\rho Cp)_h$ has been justified, the validation of the diffusion was successful. Results for various combinations of phase parameters are summarised in figure 5.3. Results are thus in good agreement with the 1D finite-difference solution. As underlined in the literature review, as it is a transient case, an asymptotic value of Nusselt number characterising the heat transfer can not be conceptually found. In other words, we can only check locally the temperature profile.

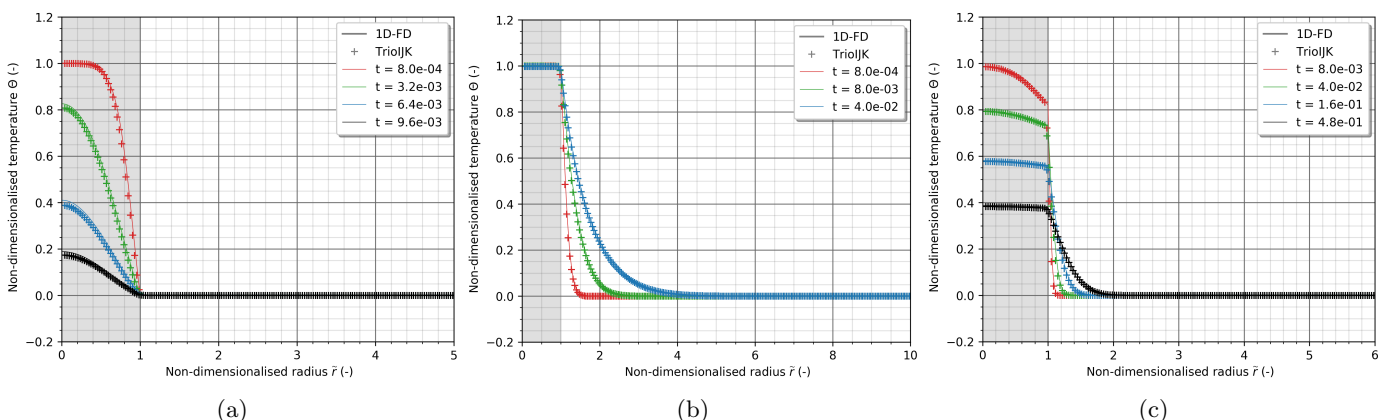


Figure 5.3: For $1/\lambda_h = \sum_k I_k^c / \lambda_k$ and $(1/\rho Cp)_h = \sum_k I_k^c / (\rho_k Cp_k)$ with $I_k^c = \int_{V_c} \chi_k dV / V_c$
 (a) Air-Water, (b) Alumina-Air , (c) Alumina-Water

An additional analysis focused on the accuracy of the prediction of interfacial properties (heat flux and temperature) as a function of time will be performed when the code capability will include the assessment of these parameters.

5.1.2 Convection validation: rising of a spherical bubble in a tri-periodic domain

The instantaneous Nusselt number for the given dynamics $Re(\mu_v/\mu_l = 0.1) = 344$ and $Re(\mu_v/\mu_l = 0.1) = 320$ is shown in Fig.5.4.a. We can notice different stages for the Nusselt number fluctuations over time. First, the Nusselt number is stable during a certain amount of time (around 0.05 seconds in this case). It corresponds to the time needed for the thermal wake of the bubble to cross the domain and impact the bubble once again i.e. $\Delta_t = l_{domain}/V_{term}$. During this amount of time, the void fraction α is not a parameter significantly influencing the heat transfer (except from its slight effect on the flow dynamics).

Then the heat transfer starts oscillating and is influenced by the void fraction, and the domain shape. This is not particularly raising our interest in the convection validation. These oscillations present negative values. It is possibly because the vapour phase has transferred its heat to the liquid and is now receiving heat from localised hot liquid zones that did not have time to be fully diffused in the rest of the liquid domain.

The Nusselt numbers have been computed using the liquid phase in the "isolated bubble" stage (i.e. the fluid with the lowest ρCp value) and their values for several Reynolds numbers are summarised in figure 5.4.b. Our numerical measurements of the Nusselt number are in good agreement with the correlation. However, we can see that they are slightly above the expected values. The correlation is not perfect in the whole range of parameters, but the value developed by the correlation is characterising the maximum reachable heat transfer for given dynamics. In our case, the bubble temperature is not fully homogeneous. It means the heat transfer should be lower than the correlation prediction. Too much energy is transferred to the liquid leading the heat transfer to be overestimated. To shine a light on

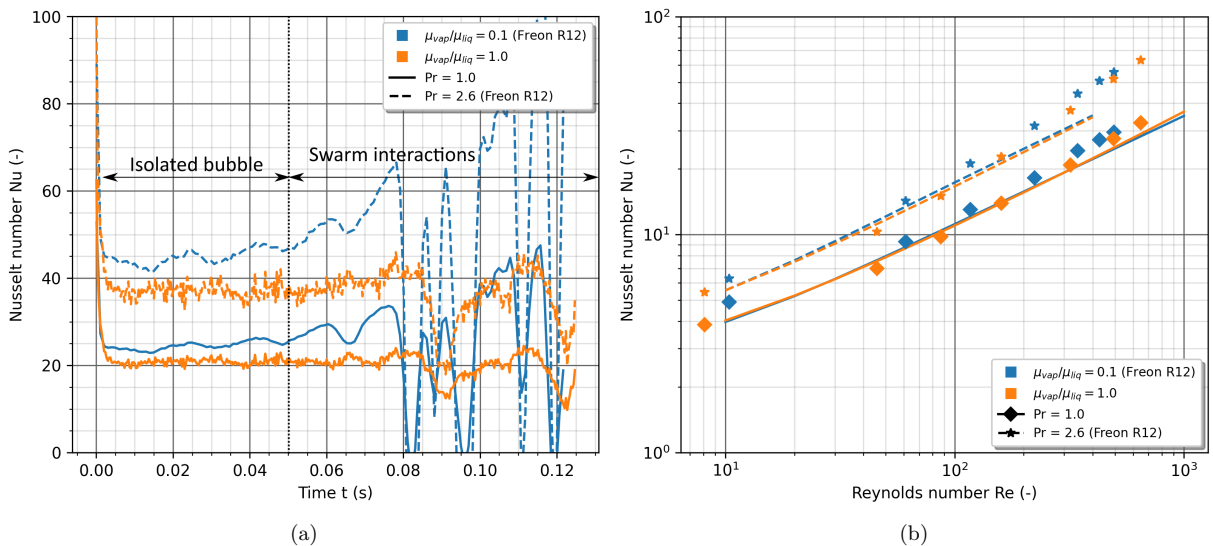


Figure 5.4: (a) Nusselt number over time for $Re(\mu_v/\mu_l = 0.1) = 344$ and $Re(\mu_v/\mu_l = 1) = 320$, $Pr_l = [1; 2.62]$ and $\mu_v/\mu_l = [0.104; 1]$
 (b) Average Nusselt number values depending on the Reynolds number

this energy leak, the same simulations have been run while disabling the diffusion (zero conductivity).

A temperature leak and consequently an energy leak has been observed (these leaks are similar to those observed in the solid body rotation test in appendix G, Fig.G.2).

It is the case in the presence of any ρCp jumps. A Nusselt number can be derived from the energy leak as shown in figure 5.5.a for $Re = 344$. It is clear that its value is not negligible and influences the results. To find its origin, we can speculate about the numerical methods used to solve the advection term.

The advection term is solved using a Quick scheme (which is inherently dissipative). As a reminder, the fluxes at the cell faces are retrieved using two upstream and one downstream points with this method. As there is a temperature gradient discontinuity at the interface, it is complicated to avoid artificial diffusion during its transport. The only way to mitigate this error is to increase the resolution to fully track the discontinuity. Doing so, it can be seen in figure 5.5.c that the Nusselt number tends towards zero for a simple translation test made by A. Sonolet when the spatial resolution is increased. Some papers involve a central differencing scheme. However, they are characterised by a high dispersion which required particular attention (Further explanations can be found in appendix G).

To correct our Nusselt number coarsely, the Nusselt number in pure advection has been measured from all the previously simulated dynamics. The values obtained have been subtracted from the previous values (from Fig.5.4.b) assuming that the purely convective case is representative of the numerical error due to convection. In fact, this correction is enveloped (a maximal bound) because the temperature gradient near the interface will always be larger in the absence of diffusion than with it. However, the correction is purely empirical as the phase temperature evolution is not the same in the case of pure advection versus the full simulation. Results are shown in figure 5.5.b. To be meticulous, the Nusselt number can conceptually be calculated only in the presence of diffusion ($Nu = f(\lambda_l)$). But instinctively, the error should be proportional to the resolution Δx and the velocity involved in each simulation. It will then give a good estimate of the error magnitude. We can see that the values of Nusselt number are now lower or almost equal to the reference provided by the correlation, as expected. An excellent agreement is obtained.

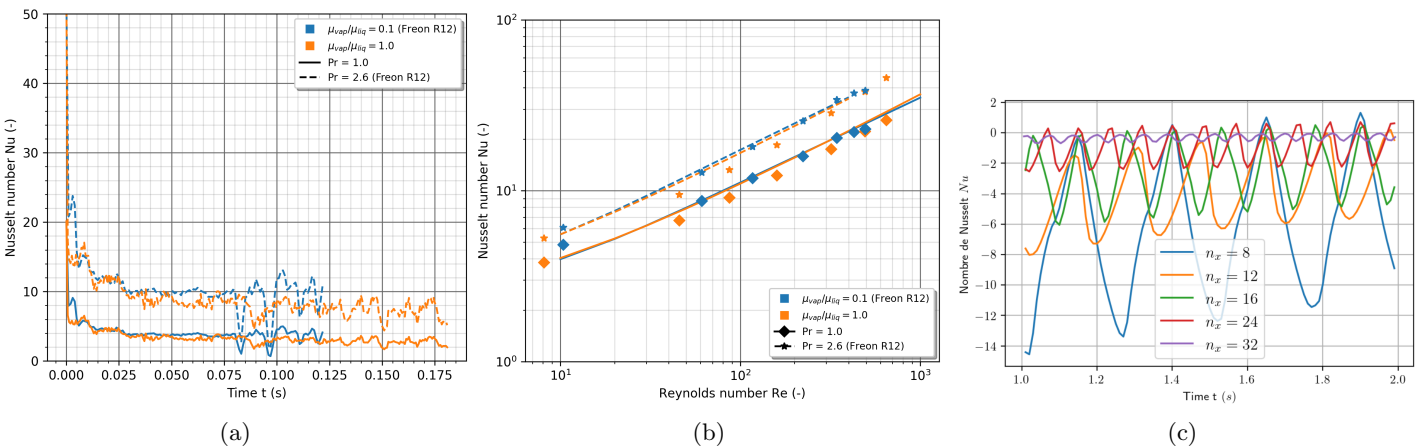


Figure 5.5: (a) Nusselt number over time without diffusion for $Re(\mu_v/\mu_l = 0.1) = 344$ and $Re(\mu_v/\mu_l = 1) = 320$, $Pr_l = [1; 2.62]$ and $\mu_v/\mu_l = [0.104; 1]$

(b) Corrected Nusselt number values depending on the Reynolds number

(c) Nusselt number values from spurious temperature leakages in pure advection and for various spatial resolution

To check the evolution of the Nusselt number with the resolution, a set of three grids is tested at a middle-range Reynolds number $Re(\mu_v/\mu_l = 0.1) = 344$. The simulations are performed with diffusion, with the set of parameters presented in table 4.2. The aim is to see if the Nusselt variations follow

a good trend i.e. if it tends to decrease with the resolution as the leakages are mitigated. We can first notice thanks to figures 5.6.a and 5.6.b, that on average, the Nusselt number decreases with an increasing resolution and the oscillations also decrease. Besides, when the liquid Prandtl number is increased, the simulation is more demanding in terms of resolution as evidenced by figure 5.6.c. It was expected as the thermal boundary layer thickness decreases with a higher liquid Prandtl value. A Prandtl value higher than 1 leads to a thermal boundary layer thinner than the velocity boundary layer.

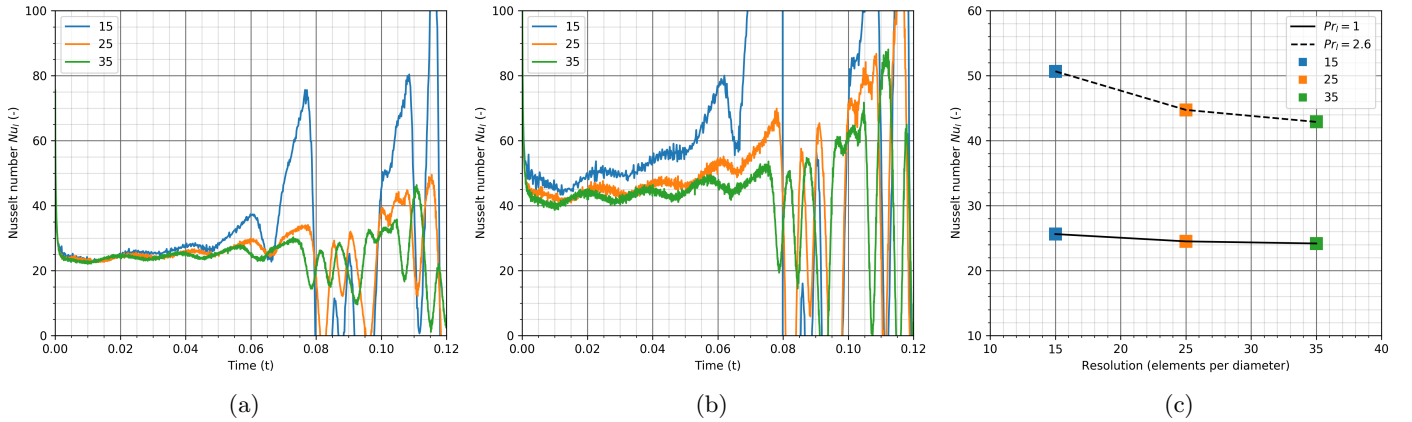


Figure 5.6: Liquid Nusselt number convergence for a set of three mesh resolutions at $Re(\mu_v/\mu_l = 0.1) = 344$ (a) $Pr_l = 1$, (b) $Pr_l = 2.6$. (c) Both Prandtl numbers
The resolution is in number of elements per diameter

We can also have a look at the difference between the Nusselt number derived from the vapour phase or from the liquid phase as shown in figure 5.7. For a Prandtl number of 1 and at a viscosity ratio of 0.1, the Nusselt number difference between both phases decreases with a better resolution, as expected, regarding the fact that the error on the energy conservation then decreases. However, if the liquid Nusselt number was almost converged with the previous grid resolutions (Fig.5.6), it is not the case for the Nusselt number derived from the evolution of energy in the vapour domain. With a relatively high resolution of 35 elements per diameter in figure 5.7.c, Nu_v is still larger than Nu_l at $Pr_l = 1$ because the contribution of vapour within the mixed cells compared to the vapour volume is much higher than that of liquid in mixed cells compared to the liquid volume. Indeed, it is related to the void fraction $\alpha = 0.8\%$ and the inter-facial area A . Consequently, the average phase temperature $\langle T \rangle_v$ is more affected by the numerical error and it may show a higher reconstruction error as well (assuming that it is localised into mixed cells). This error is only affecting the denominator of Nu_l while it is also affecting the numerator $Q_v \propto d\langle T \rangle_v/dt$ in the case of the vapour. It gives us a trail concerning the convergence of the Nusselt number which seems to depend on the resolution scaled by the proportion of the mixed cells in each phase domain. Further investigations will be required to understand better the origin of this discrepancy.

In addition, the numerical error related to the convective flux arising through the interface is expressed in temperature ($\nabla \cdot \mathbf{v}T$); thus, this numerical transfer is not preserving energy. In terms of energy, this leakage will result in higher errors on the phase with the higher ρCp (the vapour in that case). The vapour where the ρCp is the highest will show a greater energy leak. The leak, in term of energy, won't be compensated. Besides, without any ρCp jump, the energy over the domain is conserved. Consequently, the vapour showing the highest ρCp and the higher proportion of mixed cells will ineluctably show the highest error on the Nusselt number. The energy error won't be smoothed

enough by the pure vapour cells. Future works will be focused on attempting to reduce the impact of these approximations.

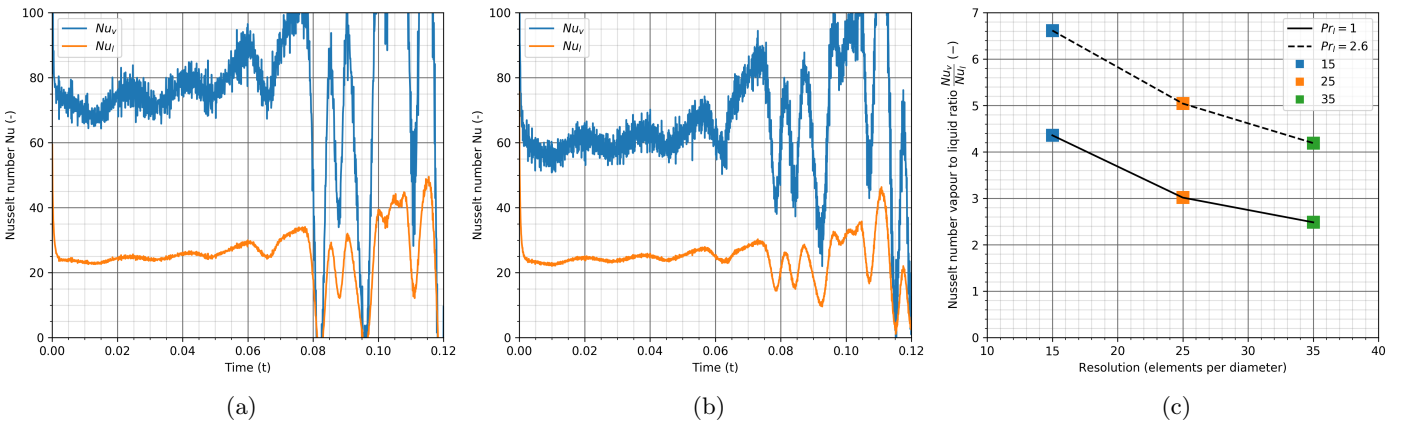


Figure 5.7: Vapour and liquid Nusselt number Nu_v and Nu_l at $Re(\mu_v/\mu_l = 0.1, Pr_l = 1) = 344$ for a resolution of 25 (a) and 35 (b) elements per diameter. (c) Nu_v to Nu_l at $Re(\mu_v/\mu_l = 0.1) = 344$ and for various resolution and liquid Prandtl number

Finally, on both figures 5.6 and 5.7, we can notice that the oscillations' amplitude during the second phase seems to be reduced with an increasing spatial resolution. If these oscillations have been partly justified by the bubble-wake interactions, they might be also caused by the previously cited numerical error. Indeed, an error in the assessment of phase temperatures may strongly impact the reconstructed Nusselt number, especially when the difference between the two temperatures becomes small. Increasing the resolution may decrease the error on the temperature difference $\langle T \rangle_v - \langle T \rangle_l$. When $(\langle T \rangle_v - \langle T \rangle_l) \rightarrow 0$, the error might be more and more visible.

A simulation involving 25 elements per diameter is already demanding in terms of calculation cost and previous dynamics studies for swarms and channels have been realised at this resolution. Solving the temperature equation is not as demanding as solving the momentum equation (Poisson solver). Besides, the transfer is settling faster than the dynamics. Consequently, it could be considered running first the dynamics at a sufficient resolution until convergence and then increased the grid resolution for the thermal study. It is the only way to ensure better results using the current implementation.

Finally, in terms of measurements strategy, the fast settling time makes it possible to run multiple thermal studies at close instants to get multiple mean values of the Nusselt number. Doing so allows reducing the uncertainty on the Nusselt number by ensemble averaging the simulations. From the set of data, the "mean of the means" and its standard deviation could be found. For a set of three measurements and for the middle resolution of 25 elements per diameter, the Nusselt number is not varying a lot. Nusselt number values of $Nu(Re = 344, \mu_v/\mu_l = 0.1, Pr_l = 1) = 24.3 \pm 0.03$ and $Nu(Re = 344, \mu_v/\mu_l = 0.1, Pr_l = 2.6) = 44.3 \pm 0.06$ have been found in a total time window of 1.3 seconds. Of course, the time window chosen to measure the average Nusselt number values may slightly affect these results.

Chapter 6

Conclusions

The implementation of the temperature equation using a one-fluid approach is not well referenced in the literature. If the continuous equation is not difficult to derive, its discretisation is more challenging. Solving the non-conservative form of the equation thanks to the current possibilities of TrioCFD platform was not as easy as expected. The transport of scalar is well documented for concentration (mass transfer) but in this case, a diffusivity analogous to $D = \lambda/(\rho Cp)$ can be used to describe the transfer; this option does not hold when the heat capacity ρCp is discontinuous. Using a non-conservative form does not ensure inherently the conservation of the energy; on the other hand, it leads to an easier formulation of the diffusion as it is associated to the temperature instead of the energy.

First, it has been shown that the choice and calculation of the one-fluid parameters λ , and ρCp should be done with attention as their calculation differs from their continuous counterparts. ρ and Cp could not be treated separately and more generally a product of one-fluid parameters can not be split unconditionally after a discretisation (or volume integration).

In pure diffusion case, it has been shown that a harmonic mean formula to calculate the averaged ρCp fraction term is compulsory when the non-conservative form is discretised. Using the arithmetic mean value of ρCp leads to an additional term in the equation, which looks proportional to a flux across the cell but cannot be rigorously expressed in terms of one-fluid variables in the general case.

Then, the conductivity jump is taken into account using a harmonic mean value of the fluids conductivities. It finds its justification in the flux conservation at the vapour/liquid interface. It has been noticed that the demonstration involves local phase temperature values instead of the one-fluid cell-averaged temperature. The temporal term is then not exactly consistent with the theoretical fluxes calculation (calculated at the cell faces). Moreover, the harmonic conductivity is only compulsory perpendicularly to the interface. An arithmetic value should be used in the tangential directions but this theoretical derivation can not be easily extrapolated for any interface orientation. The VOF/FT method comes with its approximations concerning the interface.

The results in pure diffusion have shown a good match with the "semi-analytical" ones. The diffusion case was purely radial, but instinctively, the normal component of the flux should be dominant compared to the tangential one; it should be the case in our simulation involving a boundary layer and an impermeable interface. The approximations that have been chosen are then valid and further complexity is not required.

The results for the validation of the convective term were not as conclusive as no analytical reference is available. Besides, issues of energy conservation and numerical diffusion were identified and analysed in detail. First, the energy reconstruction comes with its error. Tracking each phase's energy over time is still worth considering, but an alternative approach, consisting in computing the temperature gradient close to the interface is still in development. It will be compulsory to retrieve each phase temperature and their gradient in the mixed cells to fully characterise the unknowns in the Euler-Euler averaged

model. It will be interesting to compare this alternative to the current method for flux assessment to determine whether the current error made on the Nusselt number calculation was high using the approximation $\langle T \rangle_v \approx \langle T \rangle_l \approx \hat{T}$ in the mixed cells.

The test case to validate the convection considered the rise of a spherical bubble, at various Re and Pr numbers. The Nusselt number computed from the liquid-averaged temperature was stable for long enough to make a decent measurement. It has been shown that the averaged value was quite converged for a resolution of 25 elements per diameter which has been involved in the previous swarms' studies (dynamics only, at least for $Pr_l = 1$). However, we noticed that the Nusselt number shows oscillations after a certain period of time due to the wake interactions (periodicity of the domain) but also the numerical error related to post-processing and the solution procedure. The error made on the average phase temperature difference $\langle T \rangle_v - \langle T \rangle_l$ may become predominant when this difference decreases.

It is reasonable to say that this error mainly comes from $\langle T \rangle_v$ as it has been observed that the value of the vapour Nusselt number Nu_v is less converged than Nu_l for a given set of meshes: from coarse to fine. It has been then observed that both the reconstruction and numerical errors could be proportional to the resolution scaled by the proportion of mixed cells in the phase domain.

Even so, the results obtained through the liquid Nusselt number measurement are very satisfactory as there are matching reasonably the reference solution provided by the correlation of Feng and Michaelides [37]. The transfer is slightly overestimated because of the temperature leak from one phase to the other but increasing the resolution is mitigating this effect; additionally, we proposed a method to quantify this error induced by the convective term in order to correct the heat flux assessed.

In the future, it could be worth considering looking closely to the advection scheme which might be at the origin of the problem. Our understanding has improved and the pros and cons of the implementation; it will allow choosing each parameter deliberately to get accurate results in more complex swarms simulations. A good set of results is necessary for Aymeric Sonolet to run properly his machine learning algorithm in the prospect of developing closures for averaged two-fluid models.

Bibliography

- [1] G. Tryggvason, R. Scardovelli, and S. Zaleski. *Direct Numerical Simulations of Gas–Liquid Multiphase Flows*. Cambridge University Press, 2001.
- [2] Nithin S. Panicker, Alberto Passalacqua, and Rodney O. Fox. Computational study of the effect of homogeneous and heterogeneous bubbly flows on bulk gas–liquid heat transfer. *Journal of Fluids Engineering*, 142(10), August 2020.
- [3] G. Bois A. Du Cluzeau and A. Toutant. Analysis and modelling of bubble-induced agitation from dns of homogeneous swarms. 2020.
- [4] A. Cluzeau. Modelisation physique de la dynamique des ecolements a bulles par remontee d'echelle a partir de simulations fines. 2019.
- [5] S. Das, A. Panda, N.G. Deen, and J.A.M. Kuipers. A sharp-interface Immersed Boundary Method to simulate convective and conjugate heat transfer through highly complex periodic porous structures. *Chemical Engineering Science*, 191:1–18, 2018.
- [6] A. Panda, Y.E.J. Weitkamp, A.H. Rajkotwala, E.A.J.F. Peters, M.W. Baltussen, and J.A.M. Kuipers. Influence of gas fraction on wall-to-liquid heat transfer in dense bubbly flows. *Chemical Engineering Science: X*, 4:100037, 2019.
- [7] E.I. Thiam, E. Masi, E. Climent, O. Simonin, and S. Vincent. Particle-resolved numerical simulations of the gassolid heat transfer in arrays of random motionless particles. *Acta Mechanica*, 230(2):541–567, 2019.
- [8] L.E. Scriven. On the dynamics of phase growth. *Chemical Engineering Science*, 50(24):3905, 1995.
- [9] S. Tanguy, M. Sagan, B. Lalanne, F. Couderc, and C. Colin. Benchmarks and numerical methods for the simulation of boiling flows. *Journal of Computational Physics*, 264:1–22, 2014.
- [10] J.S. Hadamard. Mouvement permanent lent d'une sphere liquide et visqueuse dans un liquide visqueux. *C.R. Acad. Sci. Paris*, pages 1735–1752, 1911.
- [11] R. Kronig and J. Bruijsten. On the theory of the heat and mass transfer from a sphere in a flowing medium at low values of Reynolds' number. *Applied Scientific Research*, 2(1):439–446, 1951.
- [12] A. Acrivos and T.D. Taylor. Heat and mass transfer from single spheres in stokes flow. *Physics of Fluids*, 5(4):387, 1962.
- [13] A. Acrivos and J.D. Goddard. Asymptotic expansions for laminar forced-convection heat and mass transfer. *Journal of Fluid Mechanics*, 23(02):273, 1965.
- [14] A. Acrivos. A note on the rate of heat or mass transfer from a small particle freely suspended in a linear shear field. *Journal of Fluid Mechanics*, 98(2):299–304, May 1980.

BIBLIOGRAPHY

- [15] L.G. Leal. *Laminar flow and convective transport processes: scaling principles and asymptotic analysis*. Butterworth-Heinemann., 1992. OCLC: 1023394705.
- [16] E. Michaelides. *Particles, bubbles & drops: their motion, heat and mass transfer*. World Scientific, Hackensack, NJ, 2006. OCLC: ocm70861465.
- [17] V.G Levich and G. Veniamin. Physicochemical hydrodynamics. *Journal of Chemical Education*, 40(10):A827, 1962.
- [18] J. Boussinesq. Calcul du pouvoir refroidissant des fluides. *Journal de Mathmatiques Pures et Appliques*, 1:285–332, 1905.
- [19] B.P. Leclair and A.E. Hamielec. Viscous flow through particle assemblages at intermediate reynolds numbers - a cell model for transport in bubble swarms. *The Canadian Journal of Chemical Engineering*, 49(6):713–720, 1971.
- [20] S. Winnikow. Letters to the editor. *Chem. Eng. Sci.* 22, page 477, 1967.
- [21] A.E. Hamielec, A.I. Johnson, and W.T. Houghton. Numerical solution of the navier-stokes equation for flow past spheres: Part II. viscous flow around circulating spheres of low viscosity. *AICHE Journal*, 13(2):220–224, 1967.
- [22] D.W. Moore. The boundary layer on a spherical gas bubble. *Journal of Fluid Mechanics*, 16(2):161–176, 1963.
- [23] F. Takemura and A. Yabe. Gas dissolution process of spherical rising gas bubbles. *Chemical Engineering Science*, 53(15):2691 – 2699, 1998.
- [24] B. Figueroa-Espinoza and D. Legendre. Mass or heat transfer from spheroidal gas bubbles rising through a stationary liquid. *Chemical Engineering Science*, 65(23):6296–6309, December 2010.
- [25] M. Favelukis and H. Ly. Unsteady mass transfer around spheroidal drops in potential flow. *Chemical Engineering Science*, 60:7011–7021, 2005.
- [26] E. Ruckenstein. On heat transfer between vapour bubbles in motion and the boiling liquid from which they are generated. *Chemical Engineering Science*, 10(1):22 – 30, 1959.
- [27] D. Legendre and J. Magnaudet. Effet de l'acceleration d'un ecoulement sur le transfer thermique ou massique a la surface d'une bulle spherique. *C. R. ACad. Sci. Paris Srie IIb* 327, pages 63 – 70, 1999.
- [28] H. Brenner. Forced convection heat and mass transfer at small pelet numbers from a particle of arbitrary shape. *Chemical Engineering Science*, 18(2):109 – 122, 1963.
- [29] H. Kramers. Heat transfer from spheres to flowing media. *Physica*, 12(2-3):61–80, 1946.
- [30] W.E. Ranz and W.R. Marshall JR. Evaporation from drops, part i. *Chemical engineering progress*, 48(3):141 – 146, 1952.
- [31] S. Whitaker. Forced convection heat transfer correlations for flow in pipes, past flat plates, single cylinders, single spheres, and for flow in packed beds and tube bundles. *AICHE Journal*, 18(2):361–371, 1972.
- [32] J.F. Harper and D.W. Moore. The motion of a spherical liquid drop at high Reynolds number. *Journal of Fluid Mechanics*, 32(2):367–391, 1968.

- [33] M.E. Weber. Mass transfer from spherical drops at high reynolds numbers. *Industrial & Engineering Chemistry Fundamentals*, 14(4):365–366, 1975.
- [34] R. Clift, J.R. Grace, and M.E. Weber. Bubbles, drops, and particles. *Academic Press, New York*, 25(4), 1979.
- [35] R. Clift, J. Grace, and M. Weber. Bubbles, drops, and particles. 1978.
- [36] A.H. Abdel-Alim and A.E. Hamielec. A Theoretical and Experimental Investigation of the Effect of Internal Circulation on the Drag of Spherical Droplets Falling at Terminal Velocity in Liquid Media. *Industrial & Engineering Chemistry Fundamentals*, 14(4):308–312, 1975.
- [37] Z.G. Feng and E.E. Michaelides. Heat and mass transfer coefficients of viscous spheres. *International Journal of Heat and Mass Transfer*, 44(23):4445–4454, December 2001.
- [38] F. Euzenat. Simulation numerique directe et analyse des transferts de chaleur dans les lits de particules fixes et mobiles. page 267, 2017.
- [39] J. Xia, K. Luo, and J. Fan. A ghost-cell based high-order immersed boundary method for inter-phase heat transfer simulation. *International Journal of Heat and Mass Transfer*, 75(Complete):302–312, 2014.
- [40] S. Tenneti, B. Sun, R. Garg, and S. Subramaniam. Role of fluid heating in dense gassolid flow as revealed by particle-resolved direct numerical simulation. *International Journal of Heat and Mass Transfer*, 58(1-2):471–479, 2013.
- [41] R.S. Ramachandran, C. Kleinstreuer, and T.Y. Wang. Forced convection heat transfer of interacting spheres. *Numerical Heat Transfer, Part A: Applications*, 15(4):471–487, 1989.
- [42] E. Ruckenstein and E. James Davis. The effects of bubble translation on vapor bubble growth in a superheated liquid. *International Journal of Heat and Mass Transfer*, 14(7):939 – 952, 1971.
- [43] Z.G. Feng and E.E. Michaelides. Drag coefficients of viscous spheres at intermediate and high reynolds numbers. *Journal of Fluids Engineering*, 123(4):841–849, May 2001.
- [44] S.V. Patankar. *Numerical Heat Transfer and Fluid Flow*. Electro Skills Series. Hemisphere Publishing Corporation, 1980.
- [45] E. Maitre. Review of numerical methods for free interfaces. 2006.
- [46] T. Nakayama and M. Mori. An eulerian finite element method for time-dependent free surface problems in hydrodynamics. *International Journal for Numerical Methods in Fluids*, 22(3):175–194, 1996.
- [47] R. A. Gingold and J. J. Monaghan. Smoothed particle hydrodynamics: theory and application to non-spherical stars. *Monthly Notices of the Royal Astronomical Society*, 181(3):375–389, December 1977.
- [48] C.S. Peskin. Numerical analysis of blood flow in the heart. *Journal of Computational Physics*, 25(3):220–252, 1977.
- [49] M.C. Lai and Z. Li. A remark on jump conditions for the three-dimensional navier-stokes equations involving an immersed moving membrane. *Applied Mathematics Letters*, 14(2):149–154, 2001.

BIBLIOGRAPHY

- [50] C.S. Peskin. The immersed boundary method. *Acta Numerica*, 11:479–517, 2002.
- [51] J.O. Hinze. *Turbulence*. McGraw-Hill classic textbook reissue series. McGraw-Hill, 1975.
- [52] S.J. Suhas and M. Ali. Modeling transport of scalars in two-phase flows with a diffuse-interface method, 2020.

Appendix A

Overview of the numerical methods to simulate multiphase flows

To deal with interface localisation in fluid flow, methods are classified into three groups: Lagrangian, mixes of Eulerian-Lagrangian and fully Eulerian approaches. Eulerian methods involve fixed meshes *i.e.* the fluid is crossing the cells whereas the mesh cell is moving with the fluid in the case of the Lagrangian approach.

As underlined by E.Maitre [45] in his review, the modelling of interfaces implies three levels: the mathematical formulation of the phenomenon *i.e.* the flow modelling, the interface modelling and finally, some closure equations.

It is important to distinguish between the fluid flow formulation classification and the interface localisation type. Interface localisation methods are divided into two categories: front tracking where markers movement are followed in a Lagrangian way, and front capturing where the interface is built from an Eulerian quantity.

Depending on the formulations, the interface is solved implicitly in the fluid equations or on the contrary, a set of coupled equations is solved.

To summarise, Eulerian or Lagrangian can characterise both the flow modelling or the interface localisation and several combinations are possible as it will be shown in the following sub-sections.

A.1 Lagrangian and Eulerian-Lagrangian: interface tracking inherent methods

These two methods used a finite element discretisation. Pure Lagrangian flow modellings are necessarily used along with front-tracking algorithms as the entire grid is moving with the flow. Two forms of Eulerian-Lagrangian methods exist and overcome fluid-structure interactions. When a structure interacts with a fluid, the fluid boundaries may move. Consequently, the Eulerian mesh used to describe the fluid may be re-generated or deformed over time to follow the fluid domain boundaries.

A first method consists in re-meshing the entire domain at each time step and solving the equations on the initial Eulerian mesh after being mapped from the new one. The mapping from one domain to the other is done according to the interface and extrapolated to the fluid field. E.Maitre [45] underlines that it could be possible to map the flow at each instant back from a pure Lagrangian mesh but in practice, it is not a valid choice according to him.

The second approach referred to as ALE for Arbitrary Lagrangian-Eulerian is done by deforming the initial mesh from the boundary displacement. As the Eulerian mesh changes, elementary matrices need to be re-computed and spatial derivatives are difficult to obtain as it should be calculated at the same spatial point (but the mesh is moving over time) which leads to interpolations.

To summarise, using ALE approach, the Eulerian mesh can move and be adapted to the shape of the fluid domain. Besides, the mesh on the boundaries or at some interfaces is following the material motion. They are limited to moderate interfacial deformations and cannot account for topology changes

such as coalescence or break-up. By equating the Eulerian mesh motion to the material motion, it turns the approach into a Lagrangian one whether by fixing the mesh, it reduces the problem to an Eulerian formulation.

Eulerian fluid flow approaches can be combined with both interface-tracking (Lagrangian interface) and interface capturing (Eulerian interface).

A.2 Eulerian fluid flow combined with interface tracking

The most common method of interface tracking is referred to as front-tracking [1]. The interface is discretised using markers (see Fig.A.1.a) that form a mesh once triangulated. Markers need to be distributed uniformly over the interface to ensure some geometrical criteria: symmetry needs to be conserved, the outline needs to be smooth and the triangulated elements need to be well balanced (see Fig.A.1.b). All these elements are necessary to perform an accurate interface description.

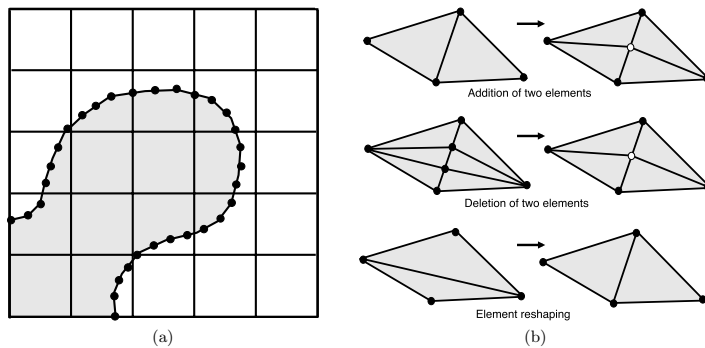


Figure A.1: Front tracking method from Tryggvason [1]: (a) Interface discretisation, (b) Elements rebalancing

However, when the markers are advected by the flow field to update their positions, the mass conservation is no longer valid as the density is a function of the marker positions. Volume variation needs thus a correction at each time-step. However, its main strength can be found in computing accurately the interface physical parameters such as the force derived from the curvature (used in the surface tension calculation). From the marker position, an Eulerian quantity can be interpolated using splines to locate the two phases in the neighbouring cells.

A second approach referred to as Volume tracking consists in placing markers within the cells where the fluid is lying [46]. In other words, the markers are superimposed on a fixed Eulerian mesh. An approximated free surface is deduced from the marker points and is thus composed of a succession of cells boundaries as shown in figures A.2a and A.2b. Three types of cells can be identified: fluid

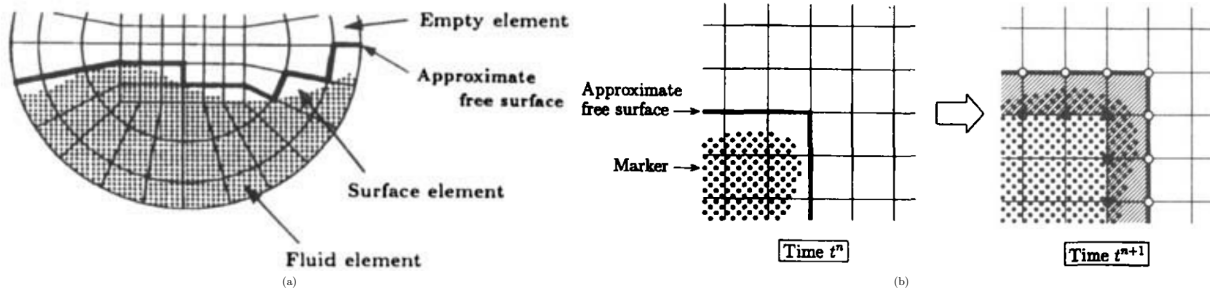


Figure A.2: Nakayama volume tracking method [46]

elements (full of markers), surface elements (partially filled) and empty elements. The fluid equations are solved on the Eulerian mesh according to the approximated free surface. The particles are then convected in a Lagrangian manner.

This method can bring others to mind like the pure Lagrangian and meshfree methods using only particles, and referred to as Smoothed-Particle Hydrodynamics (SPH) [47]. Briefly, the continuous quantities are computed from a weighted convolution of the neighbouring particle values. These methods show great advantages except concerning the treatment of boundary conditions. SPH approach will not be described extensively in this review.

The last interface-tracking method called the Immersed-Boundary Method (IBM) has been developed to deal with fluid-elastic structure interaction [48–50]. The fluid equations are solved over the entire medium. The interface is treated using a penalisation term in the momentum equation.

The structure is described by a curvilinear mesh characterised by some mechanical parameters (spring forces or bending properties) and these parameters are easily retrieved in the solver using Dirac function at the interface. By doing so, the solid behaviour can be written directly as a source term in the Navier-Stokes momentum equation.

Finally, as every previous approach, the markers are advected by the velocity field deduced from the computation of the momentum equation.

A.3 Eulerian fluid flow combined with interface capturing

The followings methods are using Eulerian fixed variables like fluid fraction inside the cell to retrieve the interface.

A first method referred to as Volume of Fluid (VOF) is formulated from the fluid fraction of each phase in each cell [1]. The fluid volume ratio over the volume of the cell (denoted α) is used to locate the interface. It can be advected as previously. The value associated to a fluid is equal to 1 in the presence of the fluid, 0 in the presence of the other fluid and between 0 and 1 when a cell is split between the two fluids as it can be seen in figure A.3.a.

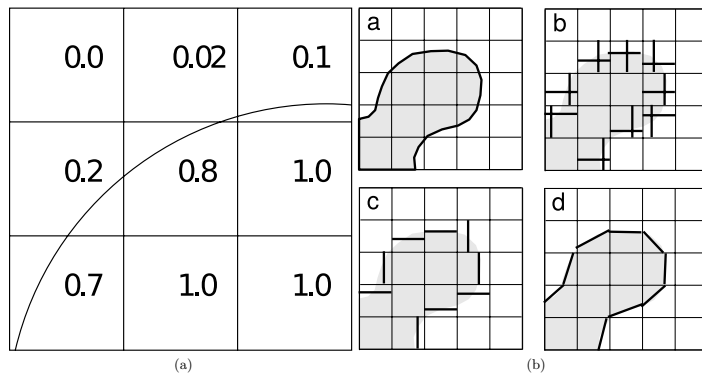


Figure A.3: (a) Fluid fraction to locate the bubble and its boundary inside the domain, (b) Original interface reconstructed using the SLIC, the Hurt and Nichols and the PLIC methods b,c and d, respectively

The interface is reconstructed using interpolation of the α field by several possible methods as it is shown in figure A.3.b. The advantage of this method is the high mass conservation accuracy obtained through the advection of the α field and its possible consistency with the discretisation of the momentum equation, thus ensuring momentum conserving schemes. However, the normal and curvature are computed at a lower order of accuracy. That is why the LMSF laboratory prefers a

combination of VOF for the location of the interface thanks to the α field and front-tracking for the computation of curvature (see Appendix B).

The Level-Set method is also particularly used to simulate bubbly flows. It relies on the declaration of a field function, commonly denoted ϕ . The interface Γ_I is represented by the zero level-set of ϕ as in figure A.4.

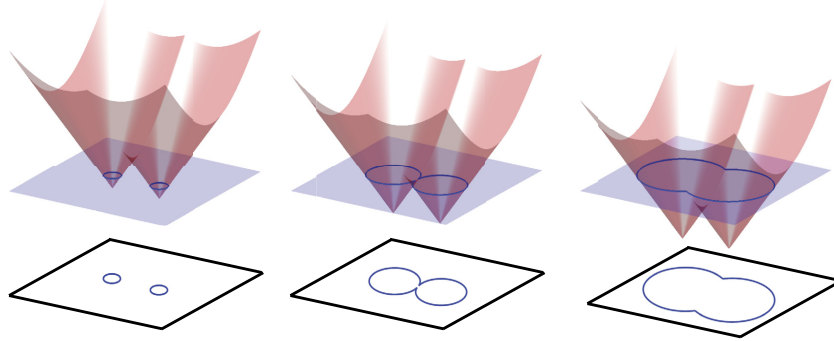


Figure A.4: Signed distance function used to represents the phase: the zero level-set corresponds to the interface. Coalescence and break-up can be modelled implicitly

The upper level-sets are representing a first fluid domain e.g. a bubble, while the lower level-sets are corresponding to the second phase. The initial function ϕ_0 is computed using a signed distance function. Inside the first fluid domain, the function has positive value and it is negative outside. Values of ϕ are then derived from the distance of each element to the initial interface Γ_0 .

The ϕ function is advected at each iteration using a transport equation $\phi_t + \mathbf{u} \cdot \nabla \phi$. The normal \mathbf{n} as well as the curvature of the surface κ can be easily computed from ϕ : $\mathbf{n} = \nabla \phi / |\nabla \phi|$ and $\kappa = \nabla \cdot \mathbf{n}$.

Hence, the inter-facial stress can be taken into account in the form of a source term using a Dirac delta function at $\phi = 0$. A marker function similar to the fluid fraction can be computed from the continuous level-set function. Contrary to the VOF method, this marker function is continuous, giving thus a smoother transition between the two fluids domains over several mesh cells [1].

Appendix B

Volume of Fluid (VOF) and Front-Tracking (FT) combination in TrioIJK

According to the methods reviewed in section 3.1, TrioIJK uses a mixed of VOF formulation and Front Tracking formulation. The initial formulation of the front-tracking method [1] uses a spline interpolation to retrieve a smoothed indicator function based on the lagrangian marker's locations compared to their neighbouring cells. Doing so, the equations are filtered so the solution obtained is not converging to the real one. In TrioIJK, the real value of the indicator function is retrieved using the interface segments between each marker. The phase indicator function field retrieved is similar to those found in VOF and allows keeping the discontinuous aspects of the interface. The general step by step algorithm can be described as follows:

- Markers position are updated (Inter-facial transport)
- Lagrangian re-meshing algorithm is performed on bubbles
- Phase indicator is updated
- Physical properties are updated based on the indicator function I_k
- Velocity is predicted
- Pressure projection is performed (Poisson solver)
- Velocity is corrected

The previous steps are performed at each time step, up to three times for sub-step schemes such as the 3rd order Runge-Kutta (RK3).

Appendix C

Two-fluid (Euler-Euler) model based on time average

C.1 Reynolds averaging in the case of single-phase flow

Turbulent fluid motion is an irregular condition of flow in which the various quantities show a random variation with time and space coordinates so that statistically distinct averaged values can be observed according to Hinze [51]. This definition of turbulence is translating the fact that transported quantities such as mass, momentum or other scalar species, fluctuate in time and space in an unsteady, random and irregular motion.

From a mathematical point of view, it implies that the instantaneous turbulent flow quantities can be split into a mean value over time and a time-dependent fluctuation value. Any transported quantity ϕ can be decomposed as $\phi(t) = \bar{\phi} + \phi'(t)$.

DNS simulations allow capturing the instantaneous fluctuations provided that the spatial resolution and time-step are sufficiently fine to take into account the whole range of fluctuation scales. As introduced in the problematic, the goal of performing DNS simulations is generally to model the Reynolds stresses denoted R_{ij} to perform statistics and calibrate averaged models.

Using a thermal analogy, the counterpart of the well-known Reynold stresses referred to as the turbulent heat flux J' could be obtained by separating T into its two contributions \bar{T} and T' and averaging the equation. This averaging is done with respect to Reynolds averaging rules: $\bar{\bar{\phi}} = \bar{\phi}$, $\bar{\phi}' = 0$ and $\bar{\phi}_1 \cdot \phi_2 = \bar{\phi}_1 \cdot \bar{\phi}_2$.

Averaging the temperature equation leads to substitute the field variables by their averaged values while adding a new term $J' = \bar{T}'\bar{v}'$ to the equation.

To begin with, we can average the temperature equation in the case of a single-phase flow as shown in equation C.1.

$$\overline{\frac{\partial \rho Cp (\bar{T} - T')}{\partial t} + \nabla \cdot [\rho Cp (\bar{T} - T') (\bar{v} + v')]} = \nabla \cdot [\lambda \nabla (\bar{T} - T')] \quad (\text{C.1})$$

The statistical average verifies the classical properties of a Reynolds averaging operator and its associated averaging rules are: $\bar{\bar{\phi}} = \bar{\phi}$, $\bar{\phi}' = 0$ and $\bar{\phi}_1 \cdot \phi_2 = \bar{\phi}_1 \cdot \bar{\phi}_2$. It leads to Eq.C.2.

$$\overline{\frac{\partial \rho Cp \bar{T}}{\partial t}} + \nabla \cdot (\rho Cp \bar{T} \bar{v}) + \cancel{\nabla \cdot (\rho Cp \bar{T}' \bar{v})} + \cancel{\nabla \cdot (\rho Cp \bar{T} v')} + \nabla \cdot (\rho Cp T' v') = \nabla \cdot (\lambda \nabla \bar{T}) \quad (\text{C.2})$$

Assuming ρ , Cp and λ constant over the phase and by re-ordering the previous equation C.2, we obtain the simplified averaged thermal convection-diffusion equation:

$$\frac{\partial \bar{T}}{\partial t} + \nabla \cdot (\bar{T} \bar{\mathbf{v}}) = \frac{1}{\rho Cp} \nabla (\lambda \nabla \bar{T}) - \nabla \cdot \bar{T}' \bar{\mathbf{v}}' \quad (\text{C.3})$$

C.2 Phase averaging

The aim of performing DNS in our case is to post-process averaged terms needed to close a two-fluid averaged model as introduced previously. Since some cells are split by the interface, doing the same averaging process in a multiphase flow implies to take into account the indicator function as follows (Favre averaging):

$$\begin{cases} \bar{\phi}_k^k = \frac{\phi_k \chi_k}{\bar{\chi}_k} \leftrightarrow \alpha_k \bar{\phi}_k^k = \bar{\phi}_k \chi_k \\ \alpha_k = \bar{\chi}_k \end{cases} \quad (\text{C.4})$$

The averaging procedure needs to be derived from equation 4.10. However, the variable decomposition into a mean and a fluctuating part is done according to the phase-averaging operator such as $\phi_k = \bar{\phi}_k^k + \phi'_k$.

Averaging rules are done according to phase k like $\bar{\phi}_k^k = \bar{\phi}_k^k$ or $\bar{\phi}'_k^k = 0$, etc. Time averaging is thus applied to the entire equation:

$$\frac{\partial (\chi_k \rho_k C p_k T_k)}{\partial t} + \nabla \cdot (\chi_k \rho_k C p_k T_k \mathbf{v}_k) = \nabla \cdot (\chi_k \lambda_k \nabla T_k) + \lambda_k \nabla T_k \cdot \mathbf{n} \delta^i \quad (\text{C.5})$$

The equation can be expressed in term of phase-averaged terms:

$$\begin{aligned} \frac{\partial (\rho_k C p_k \alpha_k \bar{T}_k^k)}{\partial t} + \nabla \cdot (\rho_k C p_k \alpha_k \bar{T}_k^k \bar{\mathbf{v}}_k^k) + \nabla \cdot (\rho_k C p_k \alpha_k \bar{T}'_k \bar{\mathbf{v}}'_k) \\ = \nabla \cdot (\lambda_k \alpha_k \bar{\nabla T}_k^k) + \lambda_k \bar{\nabla T}_k \cdot \mathbf{n} \delta^i \end{aligned} \quad (\text{C.6})$$

Finally, the temperature equation can be shorten for a better visualisation of the terms to model as in Eq.C.7.

$$\frac{\partial (\rho_k C p_k \alpha_k \bar{T}_k^k)}{\partial t} + \nabla \cdot (\rho_k C p_k \alpha_k \bar{T}_k^k \bar{\mathbf{v}}_k^k) = \nabla \cdot \left(\alpha_k \left(\bar{\mathbf{J}}_k^k - \mathbf{J}'_k \right) \right) + \bar{\mathbf{J}}_k \cdot \mathbf{n} \delta^i \quad (\text{C.7})$$

$$\text{where } \begin{cases} \mathbf{J}_k = \lambda_k \nabla T_k \\ \mathbf{J}'_k = \rho_k C p_k \bar{T}'_k \bar{\mathbf{v}}'_k \end{cases}$$

The term $\bar{\mathbf{J}}_k^k$ can be developed to highlight the averaged parameters in stake:

$$\begin{aligned} \bar{\mathbf{J}}_k^k &= \frac{\lambda_k}{\alpha_k} \bar{\chi}_k \bar{\nabla T}_k = \frac{\lambda_k}{\alpha_k} (\nabla \bar{\chi}_k \bar{T}_k - \bar{T}_k \nabla \bar{\chi}_k) = \frac{\lambda_k}{\alpha_k} \left(\nabla \left(\alpha_k \bar{T}_k^k \right) + \bar{T}_k \mathbf{n} \delta^i \right) \\ &= \frac{\lambda_k}{\alpha_k} \left(\alpha_k \nabla \bar{T}_k^k + \bar{T}_k^k \nabla \alpha_k + \bar{T}_k \mathbf{n} \delta^i \right) \\ &= \lambda_k \left(\nabla \bar{T}_k^k + \bar{T}_k^k \frac{\nabla \alpha_k}{\alpha_k} + \frac{1}{\alpha_k} \bar{T}_k \mathbf{n} \delta^i \right) \end{aligned} \quad (\text{C.8})$$

In the end, five terms $\nabla \overline{T_k}^k$, $\overline{T_k}^k \nabla \alpha_k$, $\overline{T_k \mathbf{n}_k \delta^i}$, \mathbf{J}'_k and $\overline{\mathbf{J}_k \cdot \mathbf{n}_k \delta^i}$ need to be modelled to formulate a closed-form equation. It falls to Aymeric Sonolet, the PhD student I worked with, to perform this modelling using DNS. However, to ensure the quality of the results it is essential to validate the code he implemented. If the continuous formulation of the one-fluid temperature equation is exact, its discretisation over a control volume leads to several choices having a significant impact on the accuracy of the results.

Appendix D

Thermal conductivity coefficients in normal and tangential directions to the interface

Using an arithmetic mean to calculate the average conductivity value is not consistent with the heat flux continuity in the normal direction \mathbf{n} to the interface as underlined by Patankar [44]. Using a simple 2D-configuration as shown in figure D.1, it is easy to show that the overall conductivity coefficient (between the vapour and liquid nodes v and l) should be derived from a harmonic mean formula in the normal direction to the interface.

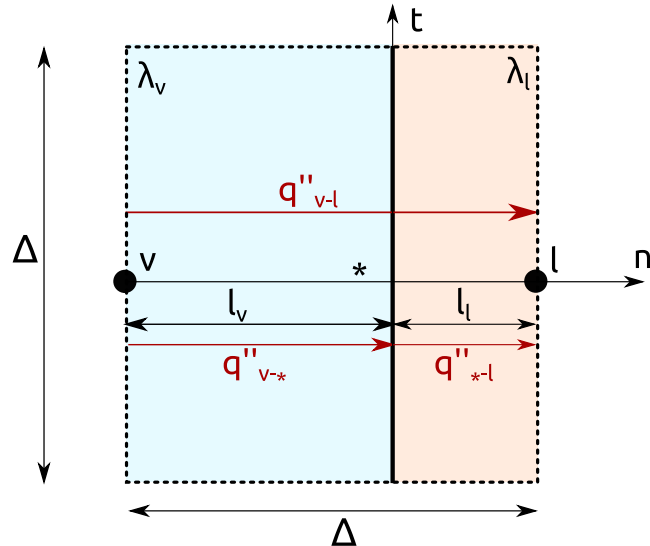


Figure D.1: Heat flux conservation in the normal direction \mathbf{n}

By calculating the heat flux balance, we can write $q'' = q''_{v-*} = q''_{*-l} = q''_{v-l}$ and their expressions:

$$\left\{ \begin{array}{l} q''_{v-*} = \frac{T_* - T_v}{l_v/\lambda_v} \\ q''_{*-l} = \frac{T_l - T_*}{l_l/\lambda_l} \\ q''_{v-l} = \frac{T_l - T_v}{(l_v + l_l)/\lambda_{eq}} = \frac{T_l - T_v}{\Delta/\lambda_{eq}} \end{array} \right. \quad (\text{D.1})$$

APPENDIX D. THERMAL CONDUCTIVITY COEFFICIENTS IN NORMAL AND TANGENTIAL DIRECTIONS TO THE INTERFACE

The temperature differences can be expressed depending on the heat flux q'' :

$$\begin{cases} q'' \frac{l_v}{\lambda_v} = T_* - T_v \\ q'' \frac{l_l}{\lambda_l} = T_l - T_* \end{cases} \quad (\text{D.2})$$

By summing the two equations, an expression of the equivalent conductivity λ_{eq} depending on each phase conductivity value can be deduced:

$$q'' = \frac{T_l - T_v}{\frac{l_v}{\lambda_v} + \frac{l_l}{\lambda_l}} \quad (\text{D.3})$$

The discretised indicator function is defined as $I_k = \int_V \chi_k dV / \int_V dV$. In the case of a 2D cubic cell of dimension Δ , we have $l_v + l_l = \Delta$, and therefore $I_k = l_k \Delta / \Delta^2 = l_k / \Delta$. So the ratio of the distance between the vapour and liquid nodes to the interface corresponds to the discretised indicator function. From $I_v = l_v / (l_v + l_l) = l_v / \Delta$ and $I_l = 1 - I_v$, we get the following expression for the equivalent conductivity λ_{eq} :

$$q'' = \frac{T_l - T_v}{(l_l + l_v) \left[\frac{I_v}{\lambda_v} + \frac{I_l}{\lambda_l} \right]} = \frac{T_l - T_v}{\Delta \left[\frac{I_v}{\lambda_v} + \frac{1 - I_v}{\lambda_l} \right]} \rightarrow \frac{1}{\lambda_{eq}} = \frac{I_v}{\lambda_v} + \frac{I_l}{\lambda_l} \quad (\text{D.4})$$

The heat through a 2D cubic cell is then $q = q'' \Delta$.

The same approach can be undertaken for the tangential conductivity coefficient in a 2D cell based on a heat balance in the tangential direction t as shown in figure D.2.

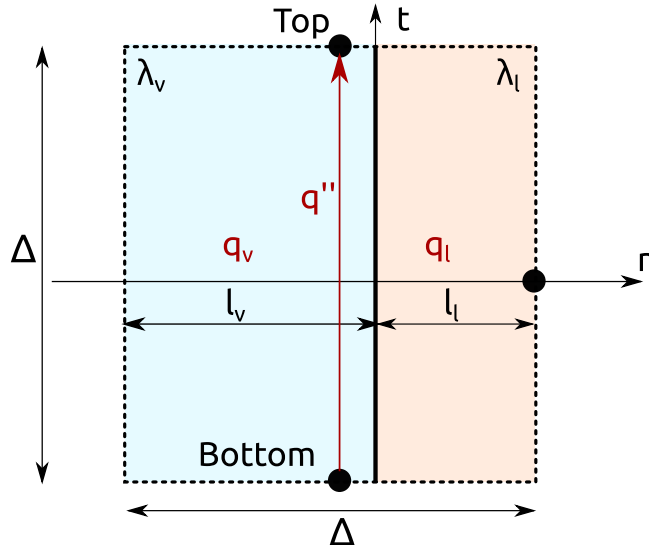


Figure D.2: Heat conservation in the tangential direction t

We can write the heat balance in the tangential direction assuming averaged temperatures on top and bottom cell faces:

$$\begin{aligned}
 q = q_v + q_l &= l_v \lambda_v \frac{T_{top} - T_{bottom}}{\Delta} + l_l \lambda_l \frac{T_{top} - T_{bottom}}{\Delta} = (\lambda_v I_v \Delta + l_l \lambda_l \Delta) \frac{T_{top} - T_{bottom}}{\Delta} \\
 &= \Delta (\lambda_v I_v + \lambda_l I_l) \frac{T_{top} - T_{bottom}}{\Delta} = \Delta \lambda_{eq} \frac{T_{top} - T_{bottom}}{\Delta}
 \end{aligned} \tag{D.5}$$

The heat flux in the tangential direction can be deduced depending on the equivalent conductivity coefficient:

$$q'' = \frac{q}{\Delta} = (\lambda_v I_v + \lambda_l I_l) \frac{T_{top} - T_{bottom}}{\Delta} \rightarrow \lambda_{eq} = \lambda_v I_v + \lambda_l I_l \tag{D.6}$$

Appendix E

ρCp justification during discretisation

E.1 Investigation of the use of an arithmetic ρCp calculation

E.1.1 Error brought by an arithmetic ρCp calculation

Starting from the temporal term of the energy equation in its conservative form (Eq.4.14), we have:

$$A = \int_{V_c} \rho CpT dV = \rho_v Cp_v \int_{V_v} T dV + \rho_l Cp_l \int_{V_l} T dV \quad (\text{E.1})$$

Using the rules $I_v^c + I_l^c = 1$, it is possible to decompose each contribution to make the arithmetic ρCp formula appear.

$$A = \rho_v Cp_v (I_v^c + I_l^c) \int_{V_v} T dV + \rho_l Cp_l (I_v^c + I_l^c) \int_{V_l} T dV \quad (\text{E.2})$$

Adding a cancelling term $B - B$ to the first equation with B showed in equation E.3, we can reveal the operator which is solved by TrioIJK and a supplementary term.

$$B = \rho_v Cp_v I_v^c \int_{V_l} T dV + \rho_l Cp_l I_l^c \int_{V_v} T dV \quad (\text{E.3})$$

It leads to equation E.4 which can be re-ordered for convenience (see Eq.E.5).

$$\underbrace{A = (\rho_v Cp_v I_v^c + \rho_l Cp_l I_l^c) \int_{V_c} T dV}_{\text{Operator solved}} + (\rho_v Cp_v - \rho_l Cp_l) \left[I_l^c \int_{V_v} T dV + I_v^c \int_{V_l} T dV \right] \quad (\text{E.4})$$

$$\int_{V_c} \rho CpT dV = \underbrace{(\rho Cp)_a \hat{T} V_c}_{\text{Solved}} + (\rho_v Cp_v - \rho_l Cp_l) I_l^c I_v^c V_c \underbrace{(\langle T \rangle_v^c - \langle T \rangle_l^c)}_{\substack{\text{Proportional to an} \\ \text{unknown flux q}}} \quad (\text{E.5})$$

E.1.2 Simplified 1D case

This section aims to develop the expression of the error using an arithmetic mean formula for the calculation of the one-fluid ρCp parameter in a simplified case (see Fig.E.1). The flux continuity at the interface expressed in the unique direction is $\lambda_v \nabla T_v = \lambda_l \nabla T_l$. Temperature T_1 and T_2 can be expressed depending on the reference temperature T_0 and the gradients ∇T_v and ∇T_l on each side on the interface i.e. thanks to the heat flux q .

$$\begin{cases} T_1 = T_0 + I_v \nabla T_v = T_0 + I_v q / \lambda_v \\ T_2 = T_1 + I_l \nabla T_l = T_1 + I_l q / \lambda_l = T_0 + q(I_v / \lambda_v + I_l / \lambda_l) \end{cases} \quad (\text{E.6})$$

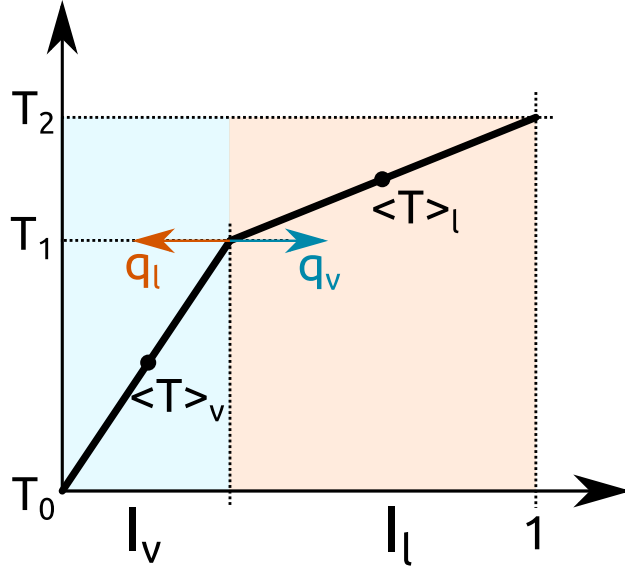


Figure E.1: Mixed cell with 1D flux $q = q_v = q_l$

Using the definition $\hat{T} = I_v^c \langle T \rangle_v + I_l^c \langle T \rangle_l$ and knowing that $\langle T \rangle_v = (T_1 + T_0)/2$, $\langle T \rangle_l = (T_2 + T_1)/2$, an energy balance on both phases can be performed and written depending on the cell average temperature \hat{T} for whom we are solving:

$$\begin{cases} E_l^c/V_c = \rho_l C p_l I_l^c \langle T \rangle_v^c = \rho_l C p_l \left[\hat{T} I_l^c + I_v^c I_l^c q / 2\lambda_h \right] \\ E_v^c/V_c = \rho_v C p_v I_v^c \langle T \rangle_l^c = \rho_v C p_v \left[\hat{T} I_v^c + I_v^c I_l^c q / 2\lambda_h \right] \end{cases} \quad (\text{E.7})$$

Finally, the total energy corresponds to the discretised equation 5.2 and the error term can be identified.

$$\hat{E}/V_c = (\rho_v C p_v I_v^c + \rho_l C p_l I_l^c) \hat{T} + [\rho C p] \frac{q}{2\lambda_h} I_l I_v = (\rho C p)_a \hat{T} + \underbrace{[\rho C p] \frac{q}{2\lambda_h} I_l I_v}_{(\rho_v C p_v - \rho_l C p_l) I_l^c I_v^c (\langle T \rangle_v^c - \langle T \rangle_l^c)} \quad (\text{E.8})$$

E.1.3 Solution with a "tweaked" initialisation and an arithmetic ρCp calculation

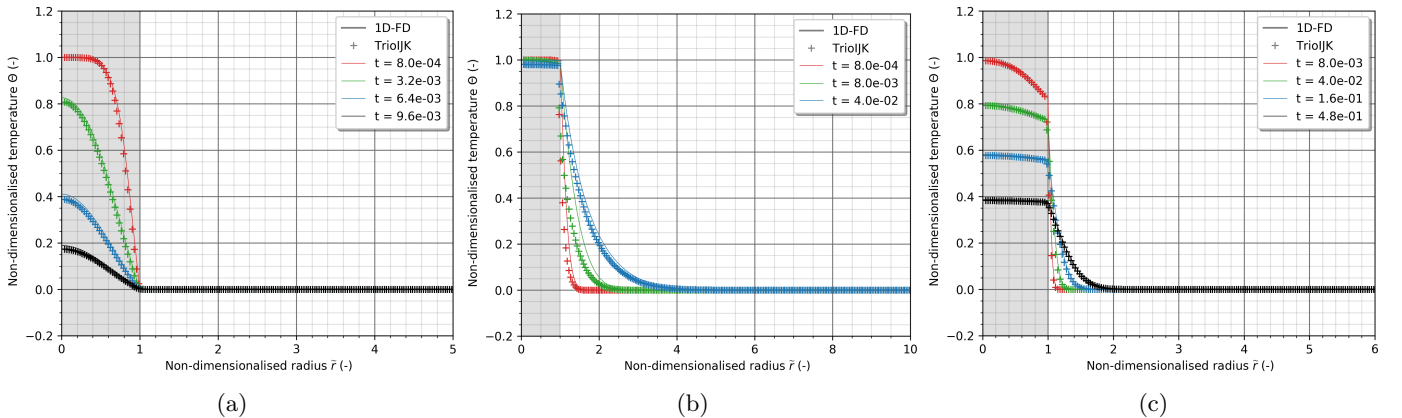


Figure E.2: Solution using a "tweaked initialisation" for $1/\lambda_h = \sum_k I_k^c / \lambda_k$ and $1/(\rho C p)_a = \sum_k I_k^c / (\rho_k C p_k)$ with $I_k^c = \int_{V_c} \chi_k dV / V_c$
 (a) Air-Water, (b) Alumina-Air , (c) Alumina-Water

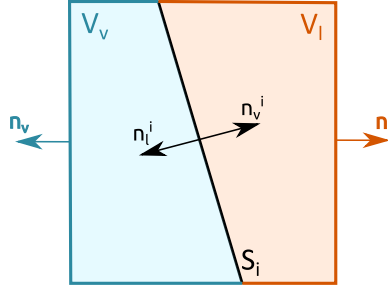


Figure E.3: Decomposition of the flux

E.2 Justification to the harmonic ρCp calculation

Starting from the diffusion term of the non-conservative form of the energy equation 4.15 and according to figure E.3, we have:

$$\int_{V_c} \frac{1}{\rho Cp} \nabla \cdot (\lambda \nabla T) dV = \frac{1}{\rho_v Cp_v} \int_{V_v} \nabla \cdot (\lambda_v \nabla T) dV + \frac{1}{\rho_l Cp_l} \int_{V_l} \nabla \cdot (\lambda_l \nabla T) dV \quad (\text{E.9})$$

It can be decomposed into a flux through the interface and those through the cell sides.

$$\underbrace{\frac{1}{\rho_v Cp_v} \int_{S_v} \lambda_v \nabla T \cdot \mathbf{n}_v dS + \frac{1}{\rho_l Cp_l} \int_{S_l} \lambda_l \nabla T \cdot \mathbf{n}_l dS}_{A = \text{Fluxes on sides}} + \underbrace{\frac{1}{\rho_v Cp_v} \int_{S_i} \lambda_v \nabla T \cdot \mathbf{n}_v^i dS + \frac{1}{\rho_l Cp_l} \int_{S_i} \lambda_l \nabla T \cdot \mathbf{n}_l^i dS}_{B = \text{Fluxes at the interface}} \quad (\text{E.10})$$

Using the rules $I_v^c + I_l^c = 1$ and $\mathbf{n}_v^i = -\mathbf{n}_l^i$, it is possible to decompose each contribution to make the harmonic ρCp formula appears. Then the term A equals:

$$A = \frac{I_v^c + I_l^c}{\rho_v Cp_v} \int_{S_v} \lambda_v \nabla T \cdot \mathbf{n}_v dS + \frac{I_v^c + I_l^c}{\rho_l Cp_l} \int_{S_l} \lambda_l \nabla T \cdot \mathbf{n}_l dS \quad (\text{E.11})$$

and B equals:

$$B = \left[\frac{1}{\rho_v Cp_v} - \frac{1}{\rho_l Cp_l} \right] \int_{S_i} \lambda \nabla T \cdot \mathbf{n}_v^i dS = \underbrace{\left[\frac{1}{\rho Cp} \right]}_{\rho Cp \text{ jump}} \int_{S_i} \lambda \nabla T \cdot \mathbf{n}_v^i dS \quad (\text{E.12})$$

A cancelling term $C - C = 0$ chosen ingeniously, with C shown in equation E.13, can be added to the initial diffusion terms A and B.

$$C = \frac{I_v^c}{\rho_v Cp_v} \int_{S_v} \lambda_l \nabla T \cdot \mathbf{n}_l dS + \frac{I_l^c}{\rho_l Cp_l} \int_{S_v} \lambda_v \nabla T \cdot \mathbf{n}_v dS \quad (\text{E.13})$$

The equation is then re-aranged to get an integral term over the total control volume $\int_S \lambda \nabla T dS$ associated to the harmonic ρCp value. It is the operator we are solving.

$$A + C - C + B = \underbrace{\left(\frac{I_v^c}{\rho_v Cp_v} + \frac{I_l^c}{\rho_l Cp_l} \right) \int_{V_c} \nabla \cdot (\lambda \nabla T) dV}_{\text{Harmonic mean of } 1/\rho Cp} \quad \text{D = Operator solved} \\ + \underbrace{\left[\frac{1}{\rho Cp} \right] \left(I_l^c \int_{S_v} \lambda_v \nabla T \cdot \mathbf{n}_v dS - I_v^c \int_{S_l} \lambda_l \nabla T \cdot \mathbf{n}_l dS + \underbrace{\int_{S_i} \lambda \nabla T \cdot \mathbf{n}_v^i dS}_{\text{Flux at the interface}} \right)}_{\text{E = supplementary term}} \quad (\text{E.14})$$

where $\left[\frac{1}{\rho Cp} \right] = \frac{1}{\rho_v Cp_v} - \frac{1}{\rho_l Cp_l}$. Finally, a supplementary term E needs to be quantified. By decomposing once again the flux at the interface using the previous indicator function rule, two terms can be highlighted.

$$E = \left[\frac{1}{\rho Cp} \right] \left[I_l^c \underbrace{\left(\int_{S_v} \lambda_v \nabla T \cdot \mathbf{n}_v dS + \int_{S_i} \lambda \nabla T \cdot \mathbf{n}_v^i dS \right)}_{\int_{V_c} \chi_v \nabla \cdot (\lambda \nabla T) dV} - I_v^c \underbrace{\left(\int_{S_l} \lambda_l \nabla T \cdot \mathbf{n}_l dS + \int_{S_i} \lambda \nabla T \cdot \mathbf{n}_l^i dS \right)}_{\int_{V_c} \chi_l \nabla \cdot (\lambda \nabla T) dV} \right] \quad (\text{E.15})$$

$\int_{V_c} \chi_k \nabla \cdot (\lambda \nabla T) dV$ is equal approximately to $V_c I_k^c \int_{V_c} \nabla \cdot (\lambda \nabla T) dV$, because of the flux continuity at the interface. The two terms corresponding to each phase fluxes balance are cancelling each others out.

$$E \approx \left[\frac{1}{\rho Cp} \right] I_l^c I_v^c V_c \left(\int_{V_c} \nabla \cdot (\lambda \nabla T) dV - \int_{V_c} \nabla \cdot (\lambda \nabla T) dV \right) = 0 \quad (\text{E.16})$$

It means that the harmonic mean formula for ρCp can be used as a one-fluid parameter to respect the fluxes balance in a mixed cell. The use of this mean formula appears then compulsory to solve the non-conservative form of the energy equation using a one-fluid approach.

$$\int_{V_c} \frac{1}{\rho Cp} \nabla \cdot (\lambda \nabla T) dV = \left(\frac{1}{\rho Cp} \right)_h \int_{V_c} \nabla \cdot (\lambda \nabla T) dV \quad (\text{E.17})$$

Appendix F

Supplementary Nusselt number values over time

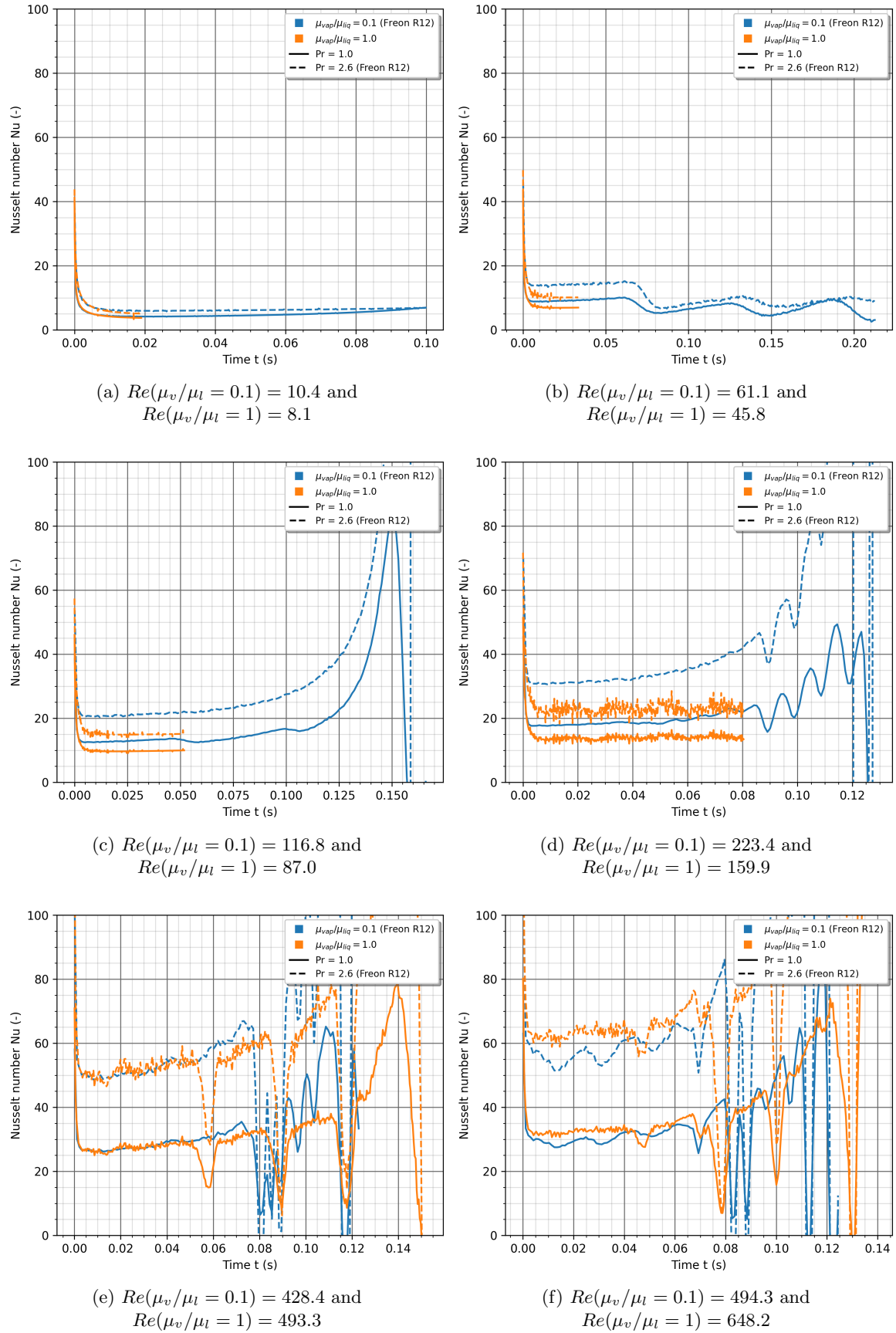


Figure F.1: Nusselt number over time for various Reynolds numbers, viscosity ratios and liquid Prandtl numbers

Appendix G

Additional observation: solid body rotation to investigate advection scheme positivity

A complementary study could be undertaken to understand deeply the effects of time and spatial schemes. It is well-known that the advection equation we are solving is showing different behaviour once discretised using various finite difference schemes. Certain schemes such as the central difference scheme can bring dispersion (oscillations) when advecting a discontinuity while numerical diffusion is inherent to upwind schemes. Moreover, the positivity of the transported scalar, that needs to be satisfied in the case of mass or temperature can be ensured according to some criteria on the time and spatial steps.

In the case of two-phase flows, the high diffusivity disparity between the two fluids makes the transport of a scalar like the mass or temperature relatively complicated to handle close to the interface. To the previously cited artefacts commonly meet, the non-sharp or diffuse interface used in VOF to conserve the scalar quantity is bringing a spurious leakage (indicator function averaged by the phase quantity in the split cells). Transport of the interface is also bringing problematics such as positivity and scalar bounds conservation.

As exposed by Jain *et al.* [52] recently, it represents a challenging task to avoid numerical leakage while keeping a positive value of the scalar. The positivity criterion sometimes referred to as "bound-edness" [44] has been investigated by Jain [52] for their phase-field approach coupled to a central difference scheme (to avoid numerical diffusion). Briefly, the phase-field method is considering an interface with a certain thickness ε . They showed that to satisfy the positivity, the spatial discretisation Δx must respect equation G.1 in addition to the Fourier number lower than 1/6:

$$\Delta x \leq \left(\frac{2D}{|u|_{max} + |u_r|_{max} + D/\varepsilon} \right) \quad (\text{G.1})$$

Where u_c , the total "convective" velocity is equal to $u + u_r$, with u the fluid velocity and u_r any effective velocity with which the scalar is advected relative to the fluid like electro-migration. In our case $u_c = u$. The criterion can be written in terms of the cell Peclet number $Pe_c = V\Delta x/D$:

$$\frac{\varepsilon}{\Delta x} \geq \frac{1 + 1/Pe_c}{2/Pe_c} \Leftrightarrow Pe_c \leq \frac{\Delta x}{2\varepsilon - \Delta x} \quad (\text{G.2})$$

For the bulk region a well-known criterion $Pe_c \leq 2$ is found and when $\varepsilon = \Delta x$, $Pe_c \leq 1$. Jain *et al.* underlines that the Fourier number value is commonly verified as the time step calculation based on the Courant number (*CFL*) is generally lower.

It could be interesting to study deeply the effect of spatial discretisation and schemes on the positivity and spurious leakages. However, by lack of time, a simple solid-body rotation with no diffusion and no

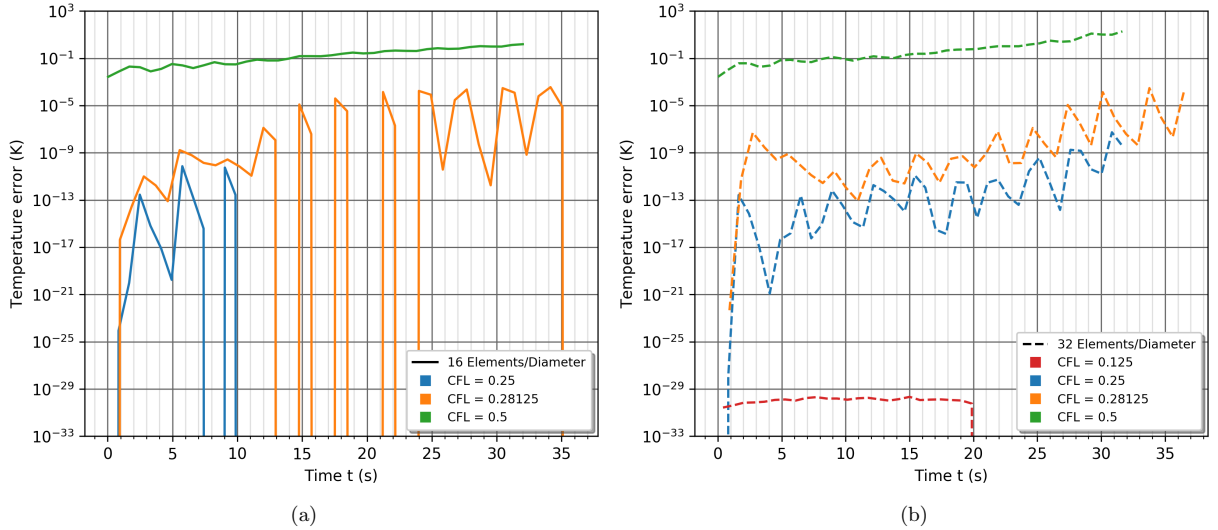


Figure G.1: Temperature values out of the bounds over time depending on the Courant number (CFL)

ρCp jumps has been investigated instead to make sure the CFL value used for dynamics is sufficiently restrictive to ensure good results. Two bubbles are initialised at a temperature $\tilde{T} = 1$. The first one is at the centre of the domain and will consequently not move. However, some leakage is expected to occur. The second one is positioned next to the first bubble and will thus rotate. In this case, the positivity will be tested. The surrounding fluid is at a temperature $\tilde{T} = 0$. Contrary to the Jain *et al.* paper, we are using a Quick scheme for the advection term. It is a high-order scheme and generally a good candidate for a low dissipative and dispersive solution. Finally, two spatial resolution have been briefly investigated: 16 and 32 elements per diameter.

For decreasing value of CFL , the minimum negative value of temperature was investigated for both spatial resolutions. First of all, it is clear that the temperature error out of the zero bound is decreasing with the CFL value as it is shown on figures G.1.a and G.1.b. It can be thus worth considering reducing the CFL number in our simulations. However, the error is keeping growing over time except for the coarser mesh at $CFL = 0.25$ and the fine one at $CFL = 0.125$. During these simulations, the error goes promptly to zero and never reappears again.

To explain this observation, we can have a look at the contour plot of the temperature over time (see figure G.2). By increasing the resolution, it is clear from figures G.2.b and G.2.d that the leakage effect will decrease. This type of numerical diffusion seems to help the temperature to remain positive.

To reduce the leakage it is then obvious to increase the resolution. However, the CFL needs to be sufficiently low to avoid a huge error outside the bounds until the numerical diffusion ensures the positivity of the solutions. The real physical diffusion process will undoubtedly help to keep the temperature between 0 and 1. Jain managed to contain the numerical diffusion of the concentration at the interface and they even achieved an impenetrable boundary condition. It could be interesting to push further this study and maybe formulate a correction in the style of previously cited Jain's papers [52]. Also, according to their criterion, a cell Peclet number lower than one seems really restrictive. For our simulation, we will keep in mind that a lower value of CFL will help to stay in the bounds and mitigating the error.

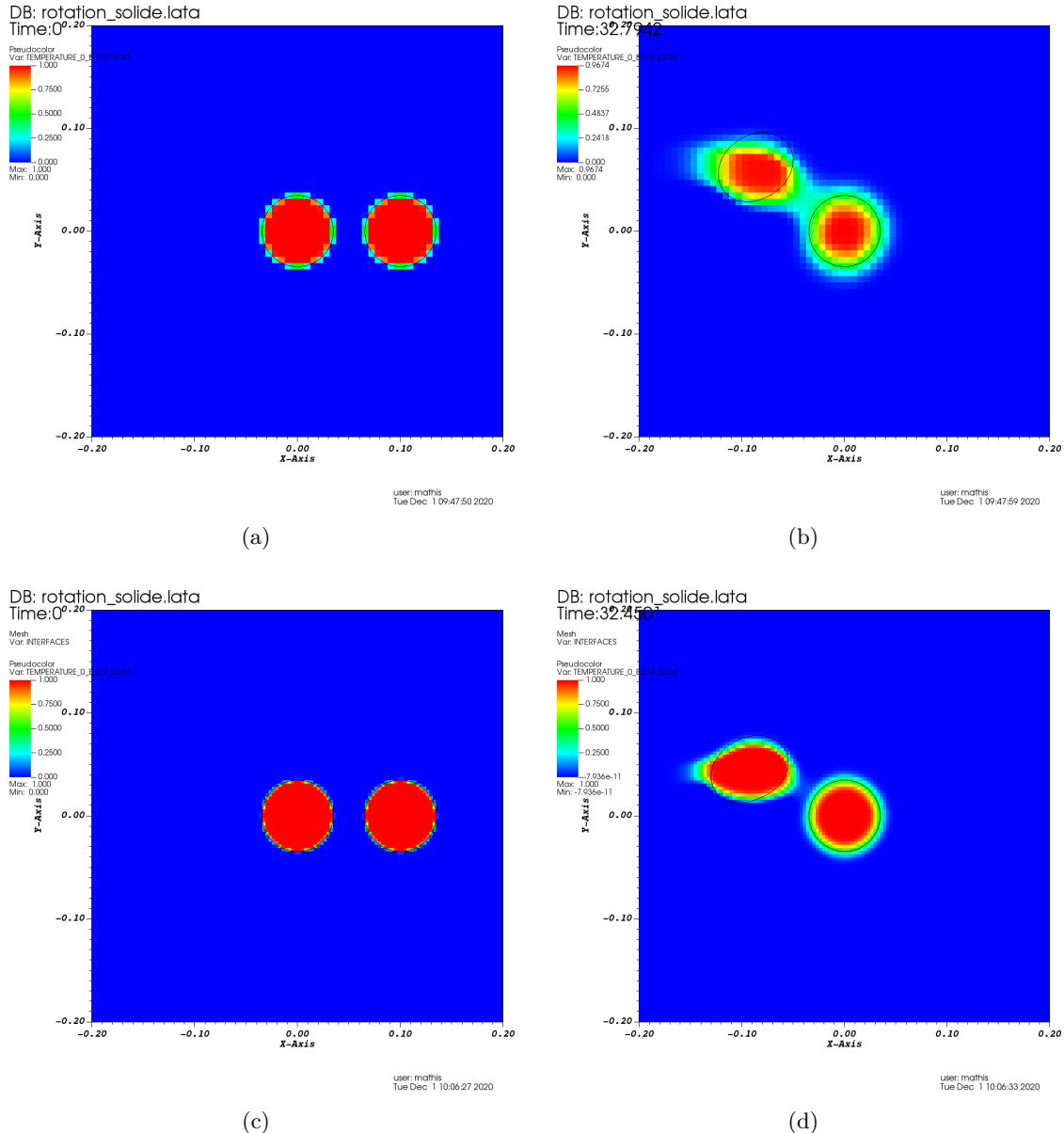


Figure G.2: Temperature distribution at the beginning and at the end of the simulation for $CFL = 0.25$:

(a) 16 elements per diameter, (b) 32 elements per diameter